

3 1176 00149 7180

UNCLASSIFIED

②

**NASA TECHNICAL
MEMORANDUM**



NASA TM X-1200
C: 2

NASA TM X-1200

CLASSIFICATION CHANGED

To **UNCLASSIFIED**

By authority of NASA LTR DTD Date Oct. 21, 1969
S/Jacob E. Smart DLG 7/10/70

**INVESTIGATION OF WATER INJECTION
ON MODELS OF GEMINI VEHICLE AND
RESULTING PREDICTIONS FOR GT-3
REENTRY COMMUNICATIONS EXPERIMENT**

*by Ivan E. Beckwith, Dennis M. Bushnell,
and Jarrett K. Huffman*
*Langley Research Center
Langley Station, Hampton, Va.*

LIBRARY COPY
MAR 7 1966
LANGLEY RESEARCH CENTER
LIBRARY, NASA
LANGLEY STATION
HAMPTON, VIRGINIA

UNCLASSIFIED

~~CONFIDENTIAL~~

UNCLASSIFIED

~~CONFIDENTIAL~~

NASA TM X-1200

CLASSIFICATION CHANGED

UNCLASSIFIED

To

By authority of NASA LTR DTD Date Oct. 21, 1969
S/Jacob E. Smart SEC 7/10/70

INVESTIGATION OF WATER INJECTION ON
MODELS OF GEMINI VEHICLE AND RESULTING PREDICTIONS
FOR GT-3 REENTRY COMMUNICATIONS EXPERIMENT

By Ivan E. Beckwith, Dennis M. Bushnell,
and Jarrett K. Huffman

Langley Research Center
Langley Station, Hampton, Va.

GROUP 4
Downgraded at 3 year intervals;
declassified after 12 years

CLASSIFIED DOCUMENT-TITLE UNCLASSIFIED

This material contains information affecting the national defense of the United States within the meaning of the espionage laws, Title 18, U.S.C., Secs. 793 and 794, the transmission or revelation of which in any manner to an unauthorized person is prohibited by law.

NOTICE

This document should not be returned after it has satisfied your requirements. It may be disposed of in accordance with your local security regulations or the appropriate provisions of the Industrial Security Manual for Safe-Guarding Classified Information.

UNCLASSIFIED

NATIONAL AERONAUTICS AND SPACE ADMINISTRATION

L-4743

~~CONFIDENTIAL~~

UNCLASSIFIED

INVESTIGATION OF WATER INJECTION ON
MODELS OF GEMINI VEHICLE AND RESULTING PREDICTIONS
FOR GT-3 REENTRY COMMUNICATIONS EXPERIMENT*

By Ivan E. Beckwith, Dennis M. Bushnell,
and Jarrett K. Huffman
Langley Research Center

SUMMARY

A wind-tunnel investigation at Mach 8 of water injection into the flow field of the Gemini reentry configuration at an angle of attack of 15° has been carried out. The maximum cross-stream penetration of the spray into the flow field was correlated in terms of model diameter, nozzle orifice diameter, water injection velocity, and stream density.

The effect of injection on surface pressures was to increase the pressure ahead of the injection site on the conical portion of the models and to decrease the pressure downstream of the injection site on the cylindrical portion. The magnitude of the change in pressure depended on the ratio of the liquid jet momentum to the momentum of the airstream flow. The effect of these pressure disturbances on the aerodynamic moments of the Gemini vehicle was estimated.

For preliminary design purposes, estimates of minimum water flow rates required to give signal recovery during the Gemini reentry were made by assuming complete evaporation of the water and chemical equilibrium composition. Three flow rates of 8.0 (3.63 kg/s), 1.3 (0.59 kg/s), and 0.3 lb/sec (0.14 kg/s) were then chosen to cover the estimated required range of rates. The wind-tunnel correlations were then used to predict the variation of maximum spray penetration with altitude and flow rate for the Gemini-Titan 3 reentry. The effect of finite evaporation rates on the two-phase flow conditions and equilibrium electron concentrations was also considered.

INTRODUCTION

The attenuation of radio communication with hypersonic reentry vehicles is known to be caused by the free electrons in the ionized flow layer that surrounds the vehicle (ref. 1, for example). When the free electron concentration exceeds some "critical" value, which for VHF transmission is about 10^9 electrons

*Title, Unclassified.

UNCLASSIFIED

~~UNCLASSIFIED~~

per cubic centimeter, the radio signal may be lost altogether depending on a number of factors other than the communication system itself. Typical of such factors are the thickness of the ionized layer and the distribution of the free electrons in the layer. On a blunt body the free electrons are produced mainly in the nose region by the bow shock, and calculations reported in reference 2 indicate that electron concentrations above the critical value would persist at large downstream distances. These calculations were made for the RAM A vehicle at a flight velocity of 17 700 feet per second (5395 m/s) and an altitude of 170 000 feet (51 816 m). This vehicle was a 9° half-angle cone with a hemispherically blunted nose of 1 inch (2.54 cm) radius.

Attenuation of radio transmission from large capsule-type vehicles, such as the Gemini and Apollo reentry modules, will be more severe than on the RAM vehicles for several reasons. First, the capsule vehicles are so much larger that the plasma layer is a few feet thick instead of a few inches thick as on the RAM vehicles. The larger extent of the normal shock in relation to the vehicle diameter due to the flatter face of the capsule vehicles also increases the relative thickness of the plasma layer. Second, over the higher altitude range which is the region of interest for the large reentry vehicles, the chemical nonequilibrium effects are more pronounced than those at the lower altitudes of the RAM flights. Third, the larger flight velocities during reentry of the capsule vehicles increase the degree of ionization and the number of gas species involved. These reasons are probably the most important ones for explaining the complete blackout of VHF transmission already observed during reentry of the Mercury vehicles from an altitude of about 300 000 feet (91 440 m) down to an altitude of 140 000 feet (42 672 m). (See ref. 3.)

It has been shown in ground facility tests (ref. 4) and in the RAM B2 flight test (ref. 5) that injection of water into the flow fields of hypersonic vehicles causes signal recovery. In the ground tests a blunted cone model with a self-contained transmitter was mounted in the exhaust from a small solid-fuel rocket motor and considerable attenuation of the radio signal was observed. When relatively small amounts of water were injected from the model into this simulated plasma, complete signal recovery was obtained. In the flight test, water was injected forward from the stagnation region and also from the sides of the vehicle just downstream of the sphere-cone shoulder. Complete or substantial recovery of the signal, which was completely lost during the no-injection periods, was observed for even the smallest flow rate of 0.04 pound per second (0.18 kg/sec).

In reference 6 studies are reported of the injection and distribution of liquids in the flow fields of sphere-cones and a Mercury model. The studies were carried out in a Mach 8 wind tunnel with the models at small or zero angles of attack. On the Mercury model the liquid was injected forward at a 65° angle to the free-stream flow direction from orifices just downstream of the heat-shield corner. The maximum penetration of the spray was correlated in terms of the liquid exit velocity, the orifice diameter, and the free-stream density and velocity. Since only one model size was used, it was not possible to determine whether the flow-field scale had any effect.

In the present investigation of water injection from the Gemini reentry shape, two model sizes have been used in an attempt to assess the effect of

UNCLASSIFIED

UNCLASSIFIED
~~CONFIDENTIAL~~

flow-field scale on the spray penetration. Also, in accordance with the flight design conditions and requirements, the wind-tunnel tests were made with the model at an angle of attack of 15° and the injection site was located on the windward side at about one-half body diameter downstream of the heat-shield corner. The water was injected forward at an angle of 25° with respect to the free-stream flow direction. This injection angle duplicated that of the flight design where forward injection was used in order to increase the dwell time of the droplets in the flow field. The purpose of the present report is to present the results of the wind-tunnel investigation of the maximum spray penetration and surface pressure distribution with water injection from the Gemini models and to indicate how these data were applied to the Gemini Titan 3 (GT-3) reentry. Some measurements showing the effect of water injection on near wake temperatures are also included.

The water flow rates used for the RAM B2 flight experiment were based primarily on equilibrium cooling considerations as discussed in detail in reference 7. Design estimates of the lower limits of flow-rate requirements for the Gemini flight experiment were based on similar considerations as discussed herein. The results of the Gemini reentry communications experiment are presented in paper 22 of reference 8, and an analysis of the flight results is given in paper 23 of reference 8. In that analysis, the experimental results of the present investigation were utilized to compute the spray area in the attached flow field and to provide an indication of the effect of water injection on the enthalpy in the separated flow region of the reentry vehicle. The analysis of reference 8 indicates that water injection reduces the free electron concentrations primarily by recombination or attachment processes that occur on or near the droplet surfaces rather than by homogeneous cooling effects.

SYMBOLS

Measurements for this investigation were taken in the U.S. Customary System of Units. Equivalent values in the International System (SI) are indicated herein in the interest of promoting use of this system in future NASA reports. Details concerning the use of SI, together with physical constants and conversion factors, are given in reference 9.

a,b,c,e	linear dimensions (see fig. 2)
C_m	moment coefficient
D	model diameter (fig. 1)
d_o	orifice diameter of nozzles (fig. 2)
f	fraction of air in approaching stream tube contained in mixing region
g,h	dimensions in figure 4

~~CONFIDENTIAL~~
UNCLASSIFIED

~~CONFIDENTIAL~~
UNCLASSIFIED

- i distance from center of windows to model injection site
- L nozzle flow length (fig. 2)
- l surface distance from heat-shield corner (fig. 1)

$$\bar{M} = \frac{\rho_l V_l^2 d_o^2}{\rho_\infty V_\infty^2 D^2} = \frac{V_l}{V_\infty} \bar{W}$$

$$M^* = (\bar{W})^{0.51} \left(\frac{V_l}{V_\infty} \right)^{0.65}$$

- \dot{m} mass flow rate
- N number of nozzles
- N_e electron density
- p pressure

$$R = \frac{r}{r_l}$$

- R_{cr} radius from aerodynamic stagnation point to streamline with $N_e = 10^9$ behind the bow shock (fig. 18)

- $R_{\infty, D}$ free-stream Reynolds number based on diameter, $\frac{\rho_\infty V_\infty D}{\mu_\infty}$

- r droplet radius

- r_{cyl} radius of cylindrical portion of vehicle

- s distance (fig. 4)

- T temperature

- t time

- V velocity

$$\bar{V} = \frac{\rho_l V_l}{\rho_\infty V_\infty}$$

$$\bar{W} = \frac{\dot{m}_c}{\dot{m}_a} = \frac{\rho_l V_l d_o^2}{\rho_\infty V_\infty D^2}$$

$$\bar{W}_{cr} = \frac{\dot{m}_c}{\pi f R_{cr}^2 \rho_\infty V_\infty}$$

- x,y Cartesian coordinate system with origin at injection point and X-axis parallel to free-stream flow direction

~~CONFIDENTIAL~~
UNCLASSIFIED

UNCLASSIFIED

~~CONFIDENTIAL~~

Z wind axis through aerodynamic stagnation point
 α angle of attack
 Δ shock stand-off distance
 β, θ angular measurements (fig. 4)
 μ viscosity
 ρ density
 ϕ angular distance around model (fig. 1)

Subscripts:

a air
c coolant or water
d droplet
l liquid at nozzle exit
m mixture of gases
max maximum spray penetration
o isentropic stagnation
o' stagnation downstream of normal shock
v vapor
w wall
wr windward ray
1 initial
2 downstream end of mixing region
 ∞ free stream ahead of bow shock
wake "near" wake of vehicle
f local flow field

~~CONFIDENTIAL~~

UNCLASSIFIED

UNCLASSIFIED

~~CONFIDENTIAL~~

APPARATUS AND TEST CONDITIONS

Wind Tunnel

The wind tunnel used in the present investigation is the same as the one used for the previous injection studies reported in reference 6. A brief description of the facility and the nominal Mach number variation is given in reference 10. In the present tests the stagnation conditions were varied from 100 psia to 2500 psia (689 475 to 17 237 500 N/m²) and from 750° F to 1050° F (671° K to 839° K). The nominal Mach number and unit Reynolds number range for these conditions is from 7.7 to 8.0 and 0.6×10^6 to 9.7×10^6 per foot (per 0.3048 m), respectively.

Models

Cutaway views of the models are shown in figure 1. The exterior shape without the sting or strut supports duplicates that of the Gemini reentry capsule. Two models were used in the investigation. The nose diameters D of these models were $1\frac{1}{2}$ (3.8 cm) and 3 inches (7.6 cm) and, as a result, these models were 1/60- and 1/30-scale models of this portion of the Gemini vehicle which has a nose diameter of 90 inches (228.6 cm).

The locations of the water injection sites and the five pressure orifices are indicated in figure 1(a). In the side-view sketch, an extended type of injection nozzle is shown mounted at $\phi = 0^\circ$. Three other injection sites located at the same l/D station but at $\phi = 20^\circ$, 40° , and 60° on the 1/30-scale model were used to obtain lateral pressure distribution data. The data were obtained by rolling the model to place an injection site on the windward streamline. (All pressure data were obtained with the model at an angle of attack of 15° .) Pressure data were then obtained at these values of ϕ by installing an injection nozzle at the windward site and by using blank plugs installed flush with the model surface at the other sites.

Some additional schlieren and spray penetration data were obtained with the 1/30-scale model supported with a side strut. A sketch of the model with the side strut attached is shown in figure 1(b). This strut configuration was used during the wake flow studies.

Water was supplied to the models by means of passages drilled in the supports. The temperature of the water inside the model was measured by a thermocouple as indicated in figure 1(a).

A sketch of the injection nozzles is shown in figure 2. Both extended and flush nozzles were used in the investigation. The L/d_0 ratio for all the nozzles was no less than 3 to minimize any effect of liquid jet area contraction. The axis of the exit passage of the nozzles was inclined at 20° from the model surface and was aligned for forward injection in a meridian plane of the model on the windward side. Each nozzle was machined to provide metal-to-metal

~~CONFIDENTIAL~~

UNCLASSIFIED

UNCLASSIFIED

~~CONFIDENTIAL~~

contact at the bottom of the hole with the correct forward alinement. This metal-to-metal contact was the only seal against water leaks; however, no leaks were observed during the course of the test program.

Water Supply System

A schematic diagram of the water supply system is shown in figure 3. The water supply tank was pressurized with nitrogen gas bottles which were attached to a common manifold. The injection pressure, as indicated by the gage just downstream of the filter, was varied from 14.7 psia (1 atmosphere) up to about 500 psia (≈ 34 atmospheres).

Visual Observation Equipment

The equipment used for observation of the liquid spray was similar to that of reference 6. A sketch of the equipment showing the approximate locations of the light source and camera with respect to the models, as positioned in the wind tunnel, is shown in figure 4. The maximum penetration and lateral distribution of the liquid spray were observed by means of a narrow light beam which originated at the light source indicated. The beam could be rotated to illuminate any section of the spray mixing region. The viewing angles of the camera with respect to the plane of the light beam were roughly 30° and 46° , as indicated in the figure for the rear-sting and side-strut supported models, respectively. These viewing angles were used to allow the lateral cross-sectional shapes of the spray region to be studied. A 35-millimeter motion-picture camera, operated at 10 frames per second, was used in the present tests. The schlieren system has been described in reference 6. Photographs were taken at 4 microseconds spark exposure with a $\frac{5}{2}$ -inch (13.97 cm) camera.

Accuracy of Instrumentation

The model surface pressures were measured with transducers that were generally accurate to within 2 percent of full-scale deflection. The measured pressures varied from about 0.1 psia (689.5 N/m^2) to 5 psia (34475 N/m^2) depending on tunnel stagnation pressure and the orifice location on the model. Transducers were available with full-scale ranges of 1, 2, and 5 psia (6895, 13790, and 34475 N/m^2); thus, by matching the transducer range to the expected pressure, the error could generally be held to less than 5 percent. However, for some of the smallest measured pressures, errors of 20 percent were possible. The model pressures were recorded on a 50-channel oscillograph.

The water pressure and tunnel stagnation pressure were measured with Bourdon dial gages that were accurate to within about $1/2$ psi (3447.5 N/m^2). These gage pressures were recorded with a 9-inch (22.86 cm) camera.

~~CONFIDENTIAL~~

UNCLASSIFIED

~~CONFIDENTIAL~~
UNCLASSIFIED

TEST PROCEDURES AND DATA REDUCTION

Spray Penetration

A typical test procedure was as follows: The supply tank was filled with water and pressurized to the desired level. The tunnel air flow was started and the model was then injected into the airstream by a movable support mechanism actuated by air cylinders. As the model was moving into the tunnel, the solenoid-actuated water valve was opened. After a time-steady spray pattern was established, the camera and recording instruments were turned on. A typical run duration was about 40 seconds.

During the run the light beam was moved fore and aft along the model flow field and the light reflected by the water spray was recorded by the motion-picture camera. The maximum spray penetration normal to the free-stream flow direction and the maximum upstream penetration were read directly from projections of the film.

The maximum spray penetration was found to depend on the water flow rate \dot{m}_c and the liquid velocity V_l at the exit of the nozzles. The nozzles and associated plumbing, as used in the tests, were calibrated to obtain \dot{m}_c as a function of the pressure drop from the injection pressure, as indicated by the gage just downstream of the filter (fig. 3), to the back pressure at the nozzle exit. Individual calibration of the nozzles as installed was necessary because of the complexity of the nozzle flow passages and other plumbing. The exit water velocity V_l as used in the correlations of the spray penetration was then computed from the formula

$$V_l = \frac{\dot{m}_c}{\rho_l \frac{\pi}{4} d_o^2}$$

Model Pressures

As mentioned previously, all pressure data were obtained with the model at an angle of attack of 15° , and with the injection nozzles on the windward ray. Also, pressure data were obtained only with the sting-supported model. (See fig. 1(a).) Surface pressure data were obtained along the windward ray over a range of tunnel stagnation pressures from 300 to 2500 psia (2 068 500 to 17 237 500 N/m²) and water tank pressures from atmospheric to 500 psia (3 447 500 N/m²). Data at values of $\phi = 20^\circ, 40^\circ$, and 60° from the windward ray were obtained by rolling the model this amount and always using the injection site that was on the windward ray. These data were obtained only for the condition of 600 psi (4 137 000 N/m²) for the tunnel stagnation pressure and 500 psi (3 447 500 N/m²) for the water tank pressure. For reference purposes, data were also obtained with no injection for the same tunnel conditions at the windward ray and at 600 psi (4 137 000 N/m²) for $20^\circ, 40^\circ$, and 60° from the windward ray.

~~CONFIDENTIAL~~
UNCLASSIFIED

UNCLASSIFIED

~~CONFIDENTIAL~~

RESULTS AND DISCUSSION

Spray Distribution and Penetration

An indication of the magnitude of flow-field disturbances due to liquid injection can be obtained from schlieren photographs. Photographs of the liquid spray as illuminated by the narrow light beam provided quantitative data on the maximum cross-current and forward penetration, and also provided an indication of the lateral distribution of the spray. In general, an oblique view of the cross-sectional shape of the spray area is available at each station because of the viewing angles of the camera with respect to the plane of the narrow light beam. These viewing angles can be obtained from the sketch and data of figure 4.

Visual data for sting-supported models.- A typical set of photographs illustrating the distribution and penetration of the liquid spray and the corresponding flow field as indicated by the schlieren photographs are shown in figures 5 and 6 for the 1/30- and 1/60-scale models with the rear sting support. Results are given for a range of relative water injection rates from $\bar{W} = 0.015$ to 0.29. Flush nozzles were used in all the data of figures 5 and 6, except figure 6(b). In these figures the upper photograph is the schlieren of the flow field. The liquid jet and some of the spray can be seen in these schlieren photographs. The lower left photograph shows the liquid spray as illuminated at a downstream station near the end of the model where on the actual vehicle the VHF antenna is located. The lower right photograph shows the spray ahead of the injection site in the vicinity of the maximum forward penetration.

Figure 5(a) is typical of "underpenetration" conditions; that is, the liquid spray penetrates only a relatively small distance into the shock layer. Figure 5(b) illustrates the penetration and spray distribution that would occur for near-optimum or "design" conditions in that most of the shock layer is penetrated by spray. The disturbance to the bow shock is still small for this case as can be seen by comparison of the schlieren with that of figure 5(a). The half-elliptical shape of the spray cross section and the concentration of spray near the body at the downstream station are typical for design conditions. Figure 5(c) shows an overpenetration case where the spray penetrates beyond the bow shock. It is of interest to note that for this case most of the spray is apparently concentrated in a region well away from the body at the downstream station. This same effect has been noted in reference 6.

Figures 6(a) and 6(b) are typical of underpenetration and design penetration conditions, respectively, for the 1/60-scale model. An extended nozzle was used for the run shown in figure 6(b). Comparison of figures 6(b) and 5(b) indicates that for similar values of the injection parameters, \bar{V} , \bar{W} , and \bar{M} , the penetration in these tests may be roughly scaled as the body size and that the extended nozzle has little apparent effect on spray distribution.

Visual data for strut-supported model.- Since the VHF antenna is located on the aft end of the Gemini reentry vehicle in a separated flow region (paper 22 of ref. 8), some data on the spray distribution in this region are

~~CONFIDENTIAL~~

UNCLASSIFIED

~~CONFIDENTIAL~~
UNCLASSIFIED

desirable. These data would assist in evaluating the effect of water injection on conditions in the separated flow region.

The strut-supported model was used to obtain these data and typical results for $\alpha = 15^\circ$ are shown in figure 7. The light beam was used to illuminate a "slice" of the spray at three axial stations of approximately $x/D = 0, 1$, and 1.35 . The data of figure 7(a) are for the injection nozzle located on the windward streamline, and for figure 7(b) the nozzle was located at $\phi = 20^\circ$ from the windward streamline. The injection nozzles on the Gemini Titan 3 vehicle were located at $\phi \approx 30^\circ$.

As would be expected, because of the streamwise momentum of the droplets, the photographs of figure 7 indicate that little, if any, spray penetrates into the separated region. Comparison of figures 7(a) and 7(b) shows that the penetration and distribution of the spray are similar for injection in the windward plane ($\phi = 0^\circ$) and off the windward plane ($\phi = 20^\circ$).

The cross-sectional shape of the water spray area can be constructed from these figures with the aid of the camera viewing angles as obtained from figure 4. Typical results at $x/D = 1.0$ and 1.35 are shown in figure 8. The elongated lobes of spray that form on either side of the separated region are caused by the cross-flow velocity components in the flow field. The resulting increase in peripheral area of the separated region that is bordered by the water spray would tend to increase the cooling effect of injection since this cooling effect depends on viscous mixing or diffusion processes that occur along the boundary of the separated region.

Maximum cross-current penetration.- Shown in figures 9(a) and 9(b) are the correlation plots of the maximum cross-current penetration y_{\max} at the x/D stations of 0 and 1.0, respectively. The correlation parameter M^* in these plots was obtained by a procedure similar to that described in reference 6. The x and y lengths used in these correlations are measured with reference to Cartesian coordinates in the plane of symmetry (pitch plane) with their origin at the exit of the injection nozzles. The X-axis is parallel to the free-stream flow direction. The station $x/D = 0$ is thus at the injection site and $x/D = 1$ is near the aft end of the vehicle where the VHF stub antenna is located. The y_{\max} is the y-coordinate of the spray "edge" as determined from spray photographs like those of figures 5 and 6.

To provide an indication of the accuracy of the correlation, all data for the 1/30- and 1/60-scale models and both flush and extended nozzles have been shown (fig. 9). Two lines of different slope have been faired through the data to indicate an apparent change in the variation of penetration with the correlating parameter that occurs when the spray reaches or exceeds the undisturbed shock location. For $x/D = 0$ and 1.0 (figs. 9(a) and 9(b)), the shock is located at $y/D = 0.59$ and 0.94 , respectively. For values of y/D greater than these values, the data appear to be correlated by lines of smaller slope. The data also exhibit larger scatter in this outer region. The increased scatter for penetration beyond the shock may be attributed partly to the increased unsteadiness of the flow, and partly to the possibility that the correlating parameter is not the best one to use for this region.

~~CONFIDENTIAL~~
UNCLASSIFIED

UNCLASSIFIED

~~CONFIDENTIAL~~

The equations for the lines shown in the plots are as follows: For $x/D = 0$ (fig. 9(a)),

$$\frac{y_{\max}}{D} = 8.19(M^*)^{0.706} \quad (y/D \leq 0.60) \quad (1)$$

$$\frac{y_{\max}}{D} = 2.07(M^*)^{0.334} \quad (y/D \geq 0.60) \quad (2)$$

For $x/D = 1.0$ (fig. 9(b)),

$$\frac{y_{\max}}{D} = 12.17(M^*)^{0.706} \quad (y/D \leq 0.94) \quad (3)$$

$$\frac{y_{\max}}{D} = 3.12(M^*)^{0.334} \quad (y/D \geq 0.94) \quad (4)$$

It is of interest to compare these results with a correlation that was derived for water injection from a Mercury model in reference 6. For the purpose of this comparison, equation (3) is written in the form

$$\frac{y_{\max}}{D} = 12.17 \bar{W}^{0.36} \left(\frac{V_l}{V_\infty} \right)^{0.46}$$

The corresponding form from reference 6 for $x/D = 1.0$ written in the notation of the present paper is

$$\frac{y_{\max}}{D} = 2.2 \bar{W}^{0.34}$$

Typical values of V_l and V_∞ for the Gemini flight experiment would be 100 ft/sec (30.48 m/s) and 24 000 ft/sec (7315.2 m/s), respectively. Inserting these values in the former equation results in values of penetration that are about one-half the values given by the latter equation from reference 6. The smaller penetration predicted by the present results is presumably due mainly to the smaller injection angle which was 25° with respect to the free-stream flow direction as compared with 65° in the Mercury tests of reference 6.

Maximum upstream penetration. - The maximum upstream penetration of the spray is correlated in figure 10 in the form of $-x_{\max}/D$ as a function of \bar{M} . This parameter \bar{M} is the ratio of the momentum flux of the liquid jet at the nozzle exit to the momentum flux of the free stream in a stream tube of diameter D .

~~CONFIDENTIAL~~
UNCLASSIFIED

~~CONFIDENTIAL~~
UNCLASSIFIED

Two lines of different slope have been used also to represent penetration within the undisturbed shock and beyond the shock. If the center-line axis of the liquid jet is extended forward, it intersects the shock at $-\frac{x}{D} = 0.53$ as indicated in the figure. The resulting equations are

$$-\frac{x_{\max}}{D} = 3.27M^{-0.34} \quad \left(-\frac{x}{D} \leq 0.53\right) \quad (5)$$

and

$$-\frac{x_{\max}}{D} = 2.51M^{-0.29} \quad \left(-\frac{x}{D} \geq 0.53\right) \quad (6)$$

Comparison of these equations with the corresponding expression of reference 6 for upstream injection from the stagnation point of a sphere-cylinder indicates that this same momentum parameter correlated those data which were for liquid nitrogen injection.

Effect of multiple injection nozzles.- All data in this report for injection from the Gemini models are for injection with a single orifice. For given stream conditions and injection direction, the penetration is controlled by the nozzle orifice diameter and the liquid velocity at the nozzle exit. If insufficient mass flow is obtained with a single nozzle of the correct diameter for penetration, it becomes necessary to use more than one or several nozzles which would be grouped close together. The question then arises as to what effect the mutual interaction between the liquid jets will have on spray penetration and distribution.

Results from a series of tests using up to three nozzles spaced a distance d_0 apart are given in the appendix. These nozzles were mounted in the floor of the Mach 8 tunnel (the same facility used in the present model tests) and were aligned to give forward injection at an angle of 20° to the stream. The cross-current penetration of the spray into the tunnel flow was correlated in terms of the orifice diameter, the free-stream density, and the water exit velocity. Comparison of this correlation with a corresponding form of the correlation derived for the Gemini scale models indicates that the cross-stream penetration is not affected by the number of jets. (See appendix.) Therefore, when the present results for cross-current penetration on the Gemini models are applied to a multiple-orifice array, the orifice diameter factors must be interpreted as the diameter of a single orifice in the array rather than any equivalent mass flow or hydraulic diameter.

Effect of Injection on Flow Field and Surface Pressures

Flow-field disturbances.- It has been shown previously that for large values of the correlating parameter, the bow shock is penetrated by the liquid jet and modified considerably. (See fig. 5(c).) The flow-field pressures and

~~CONFIDENTIAL~~

UNCLASSIFIED

UNCLASSIFIED

~~CONFIDENTIAL~~

velocities would then be modified also for this overpenetration condition. When the liquid jet and spray do not penetrate the bow shock, some flow-field disturbances can still be expected because of the presence of the jet which may not be broken up into a spray for some distance from the nozzle exit.

In figure 11, schlieren photographs of the flow field with injection and with no injection are shown. The injection case (fig. 11(a)) is for a moderate flow rate resulting in $\bar{M} = 0.00162$ and comparison with the no-injection case (fig. 11(b)) indicates that the bow shock has not been disturbed appreciably. Examination of the region between the liquid jet and the model surface in figure 11(a) indicates the presence of an oblique shock which appears to originate in the breakup region of the jet. Evidently, the liquid jet causes a disturbance in much the same manner as a solid rod of the diameter and length of the liquid jet. The flow approaching the jet is thus turned (until it is approximately parallel to the jet) by the shock originating in the breakup region. This shock interacts with the body boundary layer and is reflected back away from the surface. The reflected shock can also be seen in figure 11(a). For clarity, these features of the flow are identified in the schematic sketch of figure 11(c).

Streamwise pressure distribution.— The shock system described in the previous paragraphs causes an increase in pressure on the conical portion of the vehicle. The extent of the pressure increase would be expected to depend primarily on two variables. One of these variables is the location of the liquid jet breakup region which should vary in proportion to the forward spray penetration. The other variable is the Reynolds number because of the viscous interaction phenomenon that occurs where the shock impinges on the body boundary layer.

Pressures were measured along the windward ray over a range of stream Reynolds numbers and water flow rates. Results of these measurements are presented in figure 12 for the 1/60-scale model at $R_{\infty, D} = 3.6 \times 10^5$. Data from the 1/30-scale model at values of $R_{\infty, D}$ from 4.18×10^5 to 25.5×10^5 are shown in figure 13. In these figures, the ratio of the local measured pressure to the computed stagnation point pressure is plotted against the momentum parameter \bar{M} . This parameter is used because, as mentioned previously, the extent of the pressure disturbance should depend on the forward spray penetration which in turn depends on the momentum parameter as shown in figure 10. The data points shown at the extreme left of these figures are for zero water injection.

At the lowest Reynolds number (fig. 12), the pressure ratio at the most forward orifice a shows some increase at $\bar{M} = 7 \times 10^{-4}$. For the next two values of Reynolds number (figs. 13(a) and 13(b)) the pressure ratio at orifice a tends to increase at about $\bar{M} = 10^{-3}$ and at the highest Reynolds numbers (figs. 13(c) and 13(d)) there is no change in pressure ratio at this orifice.

At orifice b which is just upstream of the injection site the pressure increased markedly, the increase beginning somewhere in the range $3 \times 10^{-4} < \bar{M} < 7 \times 10^{-4}$. For $\bar{M} > 10^{-3}$, the pressure ratio at orifice b

~~CONFIDENTIAL~~

UNCLASSIFIED

UNCLASSIFIED

for all Reynolds numbers of these tests have increased approximately by a factor of 4, from an average of 0.045 for zero injection to 0.18 for large injection. At three of the test Reynolds numbers (figs. 12, 13(b), and 13(c)), the pressure increase apparently occurs in two steps, with an intermediate level of roughly 0.08, or almost double the zero injection level.

For increased clarity all the data from orifice b only are replotted in figure 14. The two-step nature of the pressure increase is clearly evident in this figure. The increase in pressure to the intermediate level may be associated with the interaction between the laminar boundary layer on the model and the impinging shock. A pressure increase like this increase occurs in the separation region ahead of a shock that impinges on a flat-plate laminar boundary layer (ref. 11). In the present situation, a reasonable hypothesis is that the impinging shock would move forward as \bar{M} increases and the jet penetrates farther upstream. The data show that as \bar{M} increases to about 10^{-3} , the peak pressure occurs. This peak would then correspond to the movement of the impingement region ahead of the orifice station. This hypothesis was checked by using two-dimensional oblique shock theory and assuming that the flow originally parallel to the surface is deflected 20° by the incident shock toward the surface and then deflected back parallel to the surface by the reflected shock (fig. 11). The resulting computed pressure ratio was 0.27 which is labeled in figure 14 as reflected shock pressure. The general agreement between this value and the measured pressures indicates that the hypothesis is correct. The fact that the peak measured pressures are below the computed value as well as the lack of any consistent trends with Reynolds number (as occurs on a flat plate) may be due to the three-dimensional character of the disturbance. For values of $\bar{M} > 2 \times 10^{-3}$, the spray has penetrated to the vicinity of the bow shock (see fig. 10) and the measured pressures in figure 14 tend to decrease.

By reference to figures 12 and 13 and orifice stations c, d, and e, it is seen that the pressure ratios at these stations usually tend to decrease with increasing \bar{M} (except orifice c in figs. 12 and 13(b)). This decrease in pressure ratio is the largest at station d on the cylindrical portion of the body where the no-injection pressure ratio is about twice as large as that at the other stations. This no-injection pressure ratio on the cylinder would be larger than the values on the cone because of the 20° compression at the cone-cylinder juncture. In fact, this pressure computed by assuming a two-dimensional 20° compression would be 0.134 which is somewhat higher than the measured pressure. The relatively large decreases in pressure ratio from this value for even the smallest injection rates are probably caused by a separated region downstream of the liquid jet.

Comparison of the present pressure data with that of reference 6 for water injection on the Mercury model shows an effect which may have implications regarding the effect of injection on vehicle stability. The data of reference 6 were all obtained for zero angle of attack and show that downstream of the injection site, there is generally an increase in pressure with increasing injection rates, particularly on the cylindrical portion of the model. These increases in pressure would cause a pitch-down or positive moment. The present data at $\alpha = 15^\circ$ show a decrease in pressure on the cylindrical and aft portion of the model due to injection and thus result in a pitch-up or negative moment.

UNCLASSIFIED

~~CONFIDENTIAL~~
UNCLASSIFIED

If these moments are large enough compared with those for no injection, they could result in an unstable moment variation with angle of attack. As yet, of course, this effect must be considered strictly speculative because of the different injection angle and location of the injection site in the Mercury tests. The effects of the present pressure disturbances on vehicle moments are discussed in a subsequent section.

Lateral pressure distribution.- The effect of injection on the lateral pressure distribution is shown in figure 15 where the ratio of the local pressure at $\phi = 0^\circ, 20^\circ, 40^\circ$, and 60° to the pressure for no injection at $\phi = 0^\circ$ is plotted against the ϕ angle from the windward ray. These data were obtained with the 1/30-scale model at $R_{\infty, D} = 7.15 \times 10^5$ and $\bar{M} = 2.55 \times 10^{-3}$. The flush nozzle of 0.02-inch (0.051 cm) diameter was mounted on the windward ray.

The same general trends are noted as occurred on the windward ray. The pressures at stations a and c are not affected much by injection. The large increase in pressure at station b due to injection extends around the model to about 40° from the windward ray. At stations d and e the pressures are decreased by injection and the effect extends to $\phi = 60^\circ$ and 40° , respectively.

Effect of Injection on Temperature in Separated Flow

Because of the location of the VHF antenna on the base of the Gemini reentry vehicle, radio transmission at this frequency would depend, to some extent, on the electron concentration in the separated flow region. Since the chemical and ionic species in this region are presumably in equilibrium because of the long dwell times, the electron concentration there depends only on the near wake enthalpy and pressure. Calculations made by Huber (paper 21 of ref. 8) indicate that for no water injection, the ratio of the near wake enthalpy to the stream stagnation value was approximately 0.7 on the Mercury vehicles. With water injection this ratio should be reduced, and thereby result in a corresponding reduction in electron concentration.

In order to determine an upper limit to the amount of near wake cooling caused by water injection, temperatures in the near wake of the 3-inch-diameter (7.62 cm) side-strut model were measured with and without water injection. The results of these measurements are shown in figure 16 as ratios of the wake temperature to the stream stagnation temperature. The location of the thermocouple and the tunnel conditions for the tests are given in the figure. It is seen that for the larger unit Reynolds numbers (or tunnel densities) water injection reduced the wake temperatures considerably. It should also be noted that for zero injection the wake temperature decreased with decreasing unit Reynolds number and was sensitive to the thermocouple location. Although these results cannot be applied quantitatively to the Gemini Titan 3 flight, it is clear that the measured temperature ratio in the wind-tunnel tests would represent an upper limit of the corresponding enthalpy ratio in flight. Three factors which would contribute to a larger cooling effect in flight are: (1) more of the injected water would evaporate; (2) some of the water vapor would dissociate; and (3) the wall enthalpy ratio would be smaller. Some

~~CONFIDENTIAL~~
UNCLASSIFIED

UNCLASSIFIED

~~CONFIDENTIAL~~

possible implications of the wind-tunnel test results regarding the GT-3 experiment are discussed in paper 23 of reference 8.

APPLICATION OF RESULTS TO REENTRY COMMUNICATION EXPERIMENT

The Gemini reentry communication experiment was carried out during the Gemini Titan-3 mission. Details of the results are given in paper 22 of reference 8, and a preliminary analysis of the effect of water injection on electron concentrations is given in paper 23 of reference 8. The main objectives of the experiment were to test the effectiveness of water addition for the alleviation of radio blackout on large blunt vehicles and to determine the minimum flow rates required for signal recovery. The experiment showed that water injection alleviated blackout, although, because of nonoptimum conditions, minimum flow rates were not determined.

Flight trajectory parameters for the GT-3 reentry are shown in figure 17. The altitude and velocity variations with time are shown in figure 17(a). The nominal blackout period for VHF extended from an altitude of about 318 000 feet (96 926.4 m) down to an altitude of 134 900 feet (41 117.5 m) and lasted approximately 5 minutes. Intermittent water injection was initiated at 272 270 feet (8311.9 m) and was continued down to about 160 000 feet (4876.8 m). The water was injected in short bursts of 0.1- to 0.5-second duration at intervals of approximately every 5 seconds.

Figure 17(b) shows the variation of the stream Reynolds number based on diameter of the vehicle. During the water-injection period the value of $R_{\infty,D}$ increases from about 2×10^4 to 8×10^5 . The range of Reynolds numbers covered in the present wind-tunnel tests where surface pressures were measured was $3.6 \times 10^5 \leq R_{\infty,D} \leq 2.5 \times 10^6$.

Design Estimates of Water Flow Rates

Estimates of the possible range of water flow rates to be used in the design of the injection system were initially obtained by assuming the ideal conditions of equilibrium chemistry and complete evaporation of the water in the distance from the injection site to the VHF antenna. With these assumptions, the only mechanism for electron removal would be equilibrium cooling. The injected water flow rates required to give an electron concentration N_e of 10^8 electrons per cm^3 in a mixing region of specified size and pressure were then determined. The computer program of reference 12 was used to determine the thermodynamic properties and the species present in the gas mixture after evaporation of the water. These flow rates for $N_e = 10^8$ would then be the minimum amounts required under the aforementioned ideal conditions, since recovery of a VHF signal would be obtained by reducing N_e to approximately 10^9 .

The calculation for $N_e = 10^8$ was carried out by conserving mass, momentum, and energy in a control volume described in the sketch of figure 18. All flow

UNCLASSIFIED

UNCLASSIFIED

~~CONFIDENTIAL~~

conditions at the end station 2 were assumed to be uniform in this calculation. The mass flow of free-stream air contained in the mixing region was computed from the equation

$$\dot{m}_a = \pi f R_{cr}^2 \rho_\infty V_\infty \quad (7)$$

where R_{cr} is the distance from the aerodynamic stagnation point of the vehicle to the streamline for which $N_e = 10^9$ just behind the shock, equilibrium conditions across the shock being assumed. The location of the aerodynamic stagnation point was based on the pressure distribution data of reference 13. The quantity f in equation (7) is the fraction of the incoming air in the streamtube of radius R_{cr} that is cooled to the final temperature T_2 at the downstream station. Values of f were based on the lateral extent of the spray as observed in the wind-tunnel tests (figs. 5 to 8, for example).

The bow shock shape required to determine R_{cr} was based on experimental shock shapes obtained at $M_\infty = 8$ for this body shape at angles of attack of 0° and 15° . Also used was a computed shock shape for a blunt vehicle of this type at an angle of attack of 0° and $M_\infty = 25$ (ref. 14). The shock stand-off distance for the zero angle of attack $M_\infty = 8$ case and the $M_\infty = 25$ case were plotted against the normal shock density ratio at these two conditions. On the forebody the shock stand-off distance Δ/D was measured normal to the face of the body, and on the afterbody normal to a streamwise axis Z which has its origin at the stagnation point. Straight lines connecting points at the same z/D values were drawn and it was then assumed that the slopes of these lines were invariant as the angle of attack increased to 15° . The Mach 8 data at $\alpha = 15^\circ$ were used as reference points and the shock stand-off distances at the density ratios for the Gemini flight conditions were then obtained from lines through these points with these invariant slopes. The result of this procedure is labeled in figure 18 as the estimated shock shape at 250 000 ft (76 200 m), $M_\infty = 25$. The direct use of the data of reference 13 for the aerodynamic stagnation point would give a value of $R_{cr} = 46$ inches at $\alpha = 15^\circ$. Because of the uncertainty in locating the real shock, the value of R_{cr} actually used in the calculations was 52 inches (132.08 cm) which should be conservative.

The results of the calculation with these assumed ideal conditions are shown in figure 19. The lower curve is for $N_e = 10^8$ electrons per cm^3 which was obtained at $T_2 \approx 2600^\circ \text{K}$ ($\approx 5500^\circ \text{F}$) and at mass flow ratios \bar{W}_{cr} that varied from 0.3 at the higher altitudes to 0.7 at the lower altitudes. The upper curve is for the fixed mass flow ratio $\bar{W}_{cr} = 3$ which resulted in $T_2 \approx 1800^\circ \text{K}$ ($\approx 4070^\circ \text{F}$).

Application of this same computation procedure to the RAM B2 flight conditions (ref. 7) indicated that values of $\bar{W}_{cr} \approx 0.5$ and $T_2 \approx 2200^\circ \text{K}$ (4790°F) correspond to the minimum injection rates used during the lower altitude portion of the RAM B2 test. At the highest altitudes, $\bar{W}_{cr} \approx 3.0$ would correspond to the

~~CONFIDENTIAL~~
UNCLASSIFIED

UNCLASSIFIED

~~CONFIDENTIAL~~

minimum injection rates used for that portion of the flight. Since recovery of VHF transmission was always observed during this flight even for the minimum injection flow rates, it was believed that the values of \bar{W}_{cr} and T_2 as used in the Gemini calculation would provide reasonable design estimates of the range of flow rates required for signal recovery in the Gemini experiment.

On the basis of the upper and lower curves of figure 19, three injection flow rates were chosen for the Gemini experiment. These rates were nominally 0.3, 1.3, and 8.0 lb/sec (0.14 kg/s, 0.59 kg/s, and 3.63 kg/s). According to the lower curve of figure 19, these rates would not be effective below the altitudes of 255 000 feet, 230 000 feet, and 180 000 feet (77 724 m, 70 104 m, and 54 864 m), respectively.

It is emphasized that the calculations described in this section do not in any way represent an analysis of the Gemini experiment. The calculations are included herein only to show how the original design estimates were obtained.

Spray Penetration

The maximum spray penetration at a given x station is computed from equations (1) to (4) and depends only on the shock location and the parameter M^* which is

$$M^* = \left(\frac{\rho_l V_l d_o^2}{\rho_\infty V_\infty D^2} \right)^{0.51} \left(\frac{V_l}{V_\infty} \right)^{0.65}$$

Hence, it can be seen that when the free-stream density, free-stream velocity, and the liquid velocity at the nozzle exit are known, an orifice diameter can be determined that would result in some desired penetration at a particular altitude and value of x/D . The required total mass flow could then be obtained by using more than one nozzle with this value of d_o .

The investigation of reference 6 indicated that the vapor pressure of the liquid had some effect on penetration for side (cross-current) injection. This effect was accounted for in the reference by including the ratio of vapor pressure to local flow-field pressure in the correlation parameters. For the purpose of the present investigation, this pressure ratio is taken as p_v/p_f where $p_f/p_o' = 0.05$. In the present tests p_v/p_f varied from about 1.0 to 10 and no consistent effect of this pressure ratio on penetration within the undisturbed flow field could be detected. For Gemini flight conditions, this pressure ratio would range from about 2 to 50 during the water injection experiment. Since this range exceeds that of the wind-tunnel tests, it is possible that at the higher altitudes of the flight test, the penetration predicted from equations (1) to (4) would be in some error on this account.

The desired or optimum penetration is taken as approximately 90 percent of the distance to the shock from the X-axis at both stations $x/D = 1$ and $x/D = 0$. This 90-percent figure is based on flow-field calculations similar

~~CONFIDENTIAL~~

UNCLASSIFIED

~~CONFIDENTIAL~~
UNCLASSIFIED

to those of reference 14 which indicate the values of N_e are still large enough to interfere with VHF transmission at approximately 90 percent of the shock layer thickness.

The results of the penetration calculations for the three mass flow rates and orifice diameters used are shown in figures 20(a) and 20(b) for $x/D = 0$ and $x/D = 1$, respectively. The estimated locations of the undisturbed shock for $\alpha = 15^\circ$ and 9° are also shown in these figures. The limiting values of y/D at which equations (1) to (4) were applied and the corresponding constants that were used in the equations are listed in the figure. Note that for equations (2) and (4) the constants are different from the wind-tunnel correlation values, because of the different shock locations. For $\alpha = 15^\circ$ the limiting values of y/D are based on shock stand-off distances obtained for the estimated shock of figure 18. For $\alpha = 9^\circ$ the limiting values of y/D were taken to be 24 percent greater than the values for $\alpha = 15^\circ$. This increase of 24 percent is based on the corresponding increase in shock-layer thickness observed on schlieren photographs taken during the Mach 8 wind-tunnel tests. These photographs showing the undisturbed shock (no injection) at $\alpha = 15^\circ$ and 9° are given in figure 21. (The horizontal line in these photographs is parallel to the free-stream flow direction.) The 24-percent increase in shock-layer thickness for a decrease in α from 15° to 9° is taken with respect to the same body reference line (such as the body surface) at both angles.

The penetration for the largest flow rate of 7.3 lb/sec (3.31 kg/sec) was computed by using 4 nozzles of orifice diameter $d_o = 0.221$ in. (0.56 cm). (See fig. 20.) The optimum penetration would then be achieved at an altitude of about 225 000 feet (68 580 m) for $\alpha = 15^\circ$. At higher altitudes, the penetration will be too large, and will result in inefficient use of the water. At lower altitudes, the penetration will be too small; thus, presumably an open slot or "window" across the entire plasma layer may not be achieved. The same general remarks apply to the other two flow rates of 1.48 lb/sec (0.671 kg/sec) and 0.30 lb/sec (0.136 kg/sec) for which the optimum penetration at $\alpha = 15^\circ$ would be attained at altitudes of about 240 000 feet (73 152 m) and 262 000 feet (79 857 m), respectively. Note that for these two flow rates, a single nozzle was used; thus, the optimum penetration could not be attained at any lower altitude with the given values of V_l , as shown in figure 18. The range of altitudes for optimum penetration as given above was chosen partly on the basis of the attitude of the spacecraft during a nominal reentry and the location and availability of range receiving stations during reentry.

The values of V_l , as used in the calculation, are based on total flow rate calibrations obtained with the same hardware used in flight with the final values of d_o and N as used for each flow rate. The flight system (paper 22 of ref. 8) used one supply tank pressurized to 300 lb/in² (20 685 N/m²); the values of V_l are different mainly because of different losses in the quick-opening solenoid valves.

From this discussion, it can be seen that for a fixed tank pressure and orifice diameter d_o , the optimum penetration occurs at just one altitude. This result does not imply, however, that signal recovery can be expected at only

~~CONFIDENTIAL~~
UNCLASSIFIED

UNCLASSIFIED

this one altitude. For altitudes above optimum, overpenetration occurs (fig. 20) and total mass flow requirements within the shock layer generally decrease (fig. 19); thus, for these conditions some effectiveness could be expected provided that sufficient water is deposited in the plasma layer.

The results of the GT-3 reentry communication experiment (paper 22 of ref. 8) showed that the first three large flow rates of injected water gave signal recovery on VHF. These observed signals occurred at altitudes of about 266 000 feet (81 077 m), 256 000 feet (78 029 m), and 246 000 feet (74 981 m) which are indicated in figure 20. Since the angle of attack during this portion of the reentry was approximately 9° , the upper curve would apply. According to the predictions, then, the penetration for the third pulse would have been just beyond the undisturbed shock at both $x/D = 0$ and 1. The fourth pulse at the large flow rate would have been well below the location of the undisturbed shock and as a result, marginal recovery would be expected. Since no recovery was observed for the fourth pulse, it may be concluded that the predicted values of penetration were realized to a good degree of accuracy, although underpenetration was probably not the only factor causing the lack of recovery after and including the fourth pulse. (See paper 23 of ref. 8.)

Effect of Finite Evaporation on Flow Conditions and Equilibrium N_e

The design estimates of water flow rates were based on the assumptions of equilibrium chemistry, complete evaporation between the injection site and the downstream station, and optimum location of the spray in the flow field. The effect of off-design spray penetration has been considered.

The effect of finite evaporation rates, but with equilibrium chemistry still assumed, will now be considered by means of a quasi-one-dimensional theory for liquid droplet motion and evaporation. The theory is described in detail in reference 7.

The assumption of equilibrium chemistry does not apply to neutral and ionic reactions between pure air species in the afterbody flow at high altitudes. (See paper 21 of ref. 8.) The same situation might be expected to prevail when other species are present such as those contributed by water dissociation. However, when large amounts of liquid water are injected, the flow velocity is reduced considerably and the density is increased; therefore, some reactions may tend to approach equilibrium. It is also possible that the water droplets act as catalytic centers for atom recombination. Therefore, the assumption of equilibrium chemistry may be more applicable with water injection than for the case of no injection.

The other assumptions used in the droplet theory are that uniform size droplets are formed near the injection site and thereafter the cloud of droplets is characterized by a mean droplet size and a mean velocity. The droplets are assumed to be uniformly distributed across any section. Also, the drag coefficient and Nusselt number for heat transfer as applied to the droplets in the cloud are assumed to have the same values as those for an isolated droplet at the local conditions. The initial droplet radius r_1 is computed with the

UNCLASSIFIED

~~CONFIDENTIAL~~
UNCLASSIFIED

correlations of reference 15. These correlations are based on tests made at larger densities and smaller velocities than in the present situation; however, it is believed the resulting values for r_1 are realistic on the basis of an analysis of the RAM B2 heating data with water injection (ref. 16).

The set of nonlinear equations resulting from this theoretical analysis have been programed for solution on an automatic data processing machine. Results for three altitudes that correspond approximately to the altitudes at which the optimum penetration should occur for the three flow rates (with $\alpha = 15^\circ$) are shown in figure 22. The mean flow field pressure, which is assumed to be constant in the solutions, is shown in the figures. Values of the ratio of water flow rate to airflow rate \bar{W}_{cr} which is also assumed to be constant in the mixing region, and the initial temperatures of the airstream ahead of the injection site are also shown in the figure. The values of \bar{W}_{cr} were computed in the same manner as for figure 19 with the same values of f and R_{cr} . The variations with distance downstream of the injection site of the mixture temperature T_m , mixture velocity $V_{m,x}$, equilibrium electron concentration N_e , and mass fraction of injected water still in liquid form $(r/r_1)^3 = R^3$ are shown in the figures. To illustrate the effect of initial droplet radius two different values have been used at each altitude. The largest value in each case was obtained from reference 15 for the local Gemini flow-field conditions and these results are drawn as solid lines. The other value used is $r_1 = 6.6 \times 10^{-5}$ feet or about 20 microns. The thermodynamic properties and all neutral species in the mixture were obtained with the computer program of reference 12. Since the ions are still trace species, the electron concentration was computed on the basis of the ionic reactions and the corresponding concentration of the neutrals. The only ions of any importance in the equilibrium mixture were NO^+ and OH^- .

Figures 22(a), 22(b), and 22(c) represent conditions for the 8.0 lb/sec (3.63 kg/s), 1.3 lb/sec (0.59 kg/s), and 0.3 lb/sec (0.14 kg/s), respectively. In figure 22(a), the electron concentration is already reduced below the critical value for transmission (about 8×10^8) at 0.1 foot (3.05 cm) downstream of injection where about 10 percent of the injected water is evaporated. At $x = 8$ feet (2.44 m), $N_e \approx 4 \times 10^7$ and more than 30 percent of the water is evaporated. In figure 22(b) (1.3 lb/sec case (0.59 kg/s)), the value of N_e for the large drop size reaches the critical value at $x \approx 1.0$ foot (30.5 cm) and for the small drop size the critical value of N_e is reached at about 0.4 foot (12.2 cm) from injection. About 13 percent of the injected water was evaporated for both initial drop sizes at these x-stations.

Since it is the amount of water evaporated at the 8-foot (2.44 m) station that contributes to the homogeneous cooling, it is of interest to compare these quantities with the estimated flow-rate requirements in figure 19. Also, the amounts required to give $N_e = 10^8$ are compared. The following table gives the pertinent values taken from the calculations for the largest initial drop sizes:

~~CONFIDENTIAL~~
UNCLASSIFIED

~~CONFIDENTIAL~~
UNCLASSIFIED

Figure	\dot{m}_c , lb/sec (kg/s)	Percent evaporated, $1 - R^3$		Amount evaporated, \dot{m}_v , lb/sec	
		at $x = 8$ ft (2.44 m)	at $N_e = 10^8$	at $x = 8$ ft (2.44 m)	at $N_e = 10^8$
22(a)	8.0 (3.63)	0.33	0.21	2.64 (1.20 kg/s)	1.68 (0.76 kg/s)
22(b)	1.3 (0.59)	.25	.21	.32 (0.15 kg/s)	.28 (0.13 kg/s)

These values of $\dot{m}_v = (1 - R^3)\dot{m}_c$ are plotted in figure 19 at the altitudes used. It can be seen that the amount of water evaporated and therefore available for cooling at the 8-foot (2.44 m) station is between the estimated limits for the 8.1 lb/sec (3.67 kg/s) case and somewhat below the lower limit for the 1.3 lb/sec (0.59 kg/s) case. The amounts required to give $N_e = 10^8$ are in reasonable agreement with the faired line.

Figure 22(c) represents conditions for the smallest flow rate of 0.3 lb/sec (0.15 kg/s). The value of $\bar{W}_{cr} = 0.5$ as used in the solution is slightly larger than the value that would be obtained by the use of f and R_{cr} from figure 19. Nevertheless, the computed temperature is still above 7500°R (4166°K) at $x = 8$ and $N_e \approx 5 \times 10^{10}$. About 25 percent or more of the injected water is evaporated at this station, but this amount is still insufficient to have any appreciable effect. It thus appears on the basis of finite evaporation and equilibrium cooling that 0.3 lb/sec (0.15 kg/s) flow rate would be too small to give signal recovery at this altitude.

The gas mixture velocity $V_{m,x}$ for the large and intermediate water flow rate cases (figs. 22(a) and 22(b)) is reduced by several thousand feet per second at the downstream stations near the VHF antenna site. This large reduction provides an indication of the magnitude of the droplet and gas flow interaction which may tend to cause equilibrium conditions at higher altitudes than for no injection. In the analysis of paper 23 of reference 8, the mixture composition was assumed to be frozen (except for the addition of water vapor) and the principal mechanism for electron removal was assumed to be heterogeneous reactions at or near the droplet surfaces. The result of that analysis appeared to be in reasonable agreement with experimental observations (paper 22 of ref. 8). The present equilibrium analysis does not agree quantitatively with the observed results; however, the trends with altitude and flow rate appear to be correct.

Effect of Water Injection on Vehicle Moments

The results of the wind-tunnel pressure measurements (figs. 12 to 15) indicated that for values of $\bar{M} \geq 3 \times 10^{-4}$, the pressure on the windward side of the conical portion of the test models at the orifice ahead of the injection site increased by as much as a factor of 4. Also, even for the smallest amount of injection, the pressure on the windward side of the cylindrical section decreased by about 40 percent. These pressure changes would affect the forces and moments of the flight vehicle.

~~CONFIDENTIAL~~
UNCLASSIFIED

UNCLASSIFIED

~~CONFIDENTIAL~~

To determine the severity of the problem due to pressure changes, the values of \bar{M} for the three orifice sizes to be used have been computed for the flight trajectory. The results are plotted against altitude in figure 23. From the wind-tunnel test result showing an increase in pressure on the conical section for $\bar{M} > 3 \times 10^{-4}$, it is seen that at altitudes above approximately 230 000 feet (70 104 m), 192 000 feet (58 522 m), and 165 000 feet (50 292 m) a corresponding pressure rise could occur due to injection from the nozzles of $d_o = 0.082$ (0.21 cm), 0.228 (0.58 cm), and 0.221 (0.56 cm) inch diameter, respectively. Since the water injection ended at around 160 000 feet (48 768 m), moderate to large pressure increases could occur on the conical portion of the vehicle during most of the water-on periods. Since the extent of this pressure rise may be controlled by a viscous interaction phenomenon, and since the flight Reynolds numbers (fig. 17(b)) are generally lower than the wind-tunnel test values (figs. 12 and 13), it is necessary to be conservative in applying the measured data.

To this end a maximum disturbance case was assumed wherein the pressure on the conical section forward of the injection site all the way to the forward orifice location of the present test (orifice a, fig. 1(a)), and laterally to $\phi = 45^\circ$ on either side of the windward ray increases by a factor of 3.8. This factor and the assumption of no pressure increase forward of orifice a is based on the results of the present tests (figs. 12 to 15). At the same time, the pressure on the cylindrical section to $\phi = \pm 45^\circ$ from the windward ray was assumed to decrease by 40 percent. These two pressure changes both cause a pitch-up moment and tend to increase the angle of attack. This maximum disturbance could only occur when $\bar{M} > 3 \times 10^{-4}$.

A minimum disturbance case was also assumed that corresponded to values of $\bar{M} < 3 \times 10^{-4}$. For this situation no pressure rise would occur on the conical portion (fig. 14) but the pressure decrease would still be present on the cylindrical part (figs. 12 and 13). This decrease was assumed to be 40 percent as in the maximum disturbance case. Again, in accordance with the data of figure 15, the change in pressure was assumed to extend to $\phi = \pm 45^\circ$ from the windward ray.

By using the assumed pressure distribution and the assumed areas upon which they act, a change in moment coefficient ΔC_m was calculated for both the maximum and minimum cases. The results are shown in figure 24 where the values of ΔC_m are applied to the moment coefficient curve for the Gemini configuration from reference 17.

These maximum and minimum changes in moment coefficient are highly conservative due to the following: (a) For the actual flight experiment injection is at $\phi = 30^\circ$ instead of at the windward ray, and therefore the pressure levels would probably be lower than assumed. (b) The results shown in figure 15(b) indicate that the pressure would not remain constant at the windward ray level along the conical portion for ϕ greater than about 20° .

Computations (unpublished) on the motions of the spacecraft due to these maximum and minimum ΔC_m values have been made and analyzed by Thomas M. Walsh of Langley Instrument Research Division. These ΔC_m values were assumed to be

~~CONFIDENTIAL~~

UNCLASSIFIED

UNCLASSIFIED

~~CONFIDENTIAL~~

constant in the analysis and the results indicated that for the short injection periods used, the spacecraft motions would be small.

CONCLUDING REMARKS

Wind-tunnel tests have been carried out to provide design parameters for the Gemini reentry communication experiment. The general problem areas investigated in the tests were the penetration of the liquid spray into the flow field and the effect of injection on vehicle surface pressure. Estimated design limits for water flow rates required for signal recovery on the basis of complete and partial evaporation and equilibrium properties are included. All pressure tests were made with the model at an angle of attack of 15° . The water was injected from a single nozzle located on the windward side of the conical portion of the model. The nozzle was oriented to inject the water upstream at an angle of 20° with respect to the model surface.

The liquid spray penetration into the flow field was correlated in terms of model diameter, nozzle orifice diameter, liquid exit velocity, and free-stream density. The correlating expression was found to change when the spray penetrated beyond the location of the undisturbed bow shock. The correlations were used to predict the variation with altitude and flow rate of the spray penetration for the Gemini Titan 3 (GT-3) reentry. The observed signal recovery for VHF during the flight experiment indicated that the predicted spray penetration was verified to a good degree of accuracy.

The effect of water injection on surface pressures was to increase the pressure ahead of the injection site on the conical portion of the models by as much as 300 percent, depending on the value of a momentum parameter \bar{M} . This parameter is the ratio of the momentum of the liquid jet at the nozzle exit to the momentum of the incoming air in a stream tube of model nose diameter. For $\bar{M} \geq 3 \times 10^{-4}$, the pressure ahead of the injection site began to rise and reached a peak of about four times the undisturbed level at $\bar{M} \approx 2 \times 10^{-3}$. The pressure increases were apparently caused by the interaction with the body of a shock generated by the liquid jet. The pressure downstream of the injection site on the cylindrical portion of the vehicle was decreased by about 40 percent for all injection flow rates tested. These pressure disturbances extended around the vehicle no more than 45° to either side of the windward ray. The effects of the pressure disturbances on the aerodynamic moment of the flight vehicle were estimated.

Three water flow rates of approximately 8.0 lb/sec (3.63 kg/s), 1.3 lb/sec (0.59 kg/s), and 0.3 lb/sec (0.14 kg/s) were chosen for the flight experiment to cover the estimated range required. At the "design" altitudes where the optimum penetration was predicted, these flow rates were analyzed on the basis of finite evaporation rates with equilibrium cooling. The results indicated that N_e would be reduced to the critical level for transmission of about 8×10^8 at downstream distances from injection of about 0.1 foot (0.03 m) and 1 foot (0.3 m) for the largest and intermediate rates, respectively. For the small flow rate, $N_e \approx 10^{10}$ at 10 feet (3.05 m) from injection and indicates

~~CONFIDENTIAL~~

UNCLASSIFIED

~~CONFIDENTIAL~~
UNCLASSIFIED

that no recovery of radio transmission could be expected for the small flow rate at the design altitude. Because of a general reduction in flow rate requirements with increasing altitude, some increase in effectiveness could occur at altitudes above the design values.

The VHF antenna on the Gemini reentry configuration is located on the base of the vehicle in a region of separated flow. The flow conditions in this region during injection cannot be computed; however, wind-tunnel data indicate that some cooling effects would be expected.

Langley Research Center,
National Aeronautics and Space Administration,
Langley Station, Hampton, Va., October 11, 1965.

~~CONFIDENTIAL~~
UNCLASSIFIED

UNCLASSIFIED

APPENDIX

EFFECT OF MULTIPLE INJECTION NOZZLES ON PENETRATION

The wind-tunnel tests used to determine spray penetration correlations for the Gemini scale models were carried out with single injection orifices. In order to obtain the desired penetration for the GT-3 experiment at the lower altitudes for the large injection flow rate, it was necessary to use four orifices of 0.221-inch (0.56 cm) diameter. Since this predicted penetration was based on the wind-tunnel tests with a single orifice, it was necessary to determine the effect of multiple orifices (spaced close together at an injection site) on penetration.

Apparatus

The Gemini scale models and injection nozzles (figs. 1 and 2) were too small for the convenient installation of multiple orifice nozzles. Hence, this investigation was done by means of injection nozzles installed in a curved plate that was mounted flush with the wall of the Mach 8 variable density wind tunnel (the same facility as that used for the scale model tests).

A sketch of the plate showing the nozzle installation is given in figure 25. Details of the test nozzles are also shown in the figure. These nozzles were screwed into the end of a 1.06-inch-diameter (2.69 cm) pipe that was attached to the bottom of the plate at an angle of 20° with the plate surface, as illustrated. This injection angle, and the recessed mounting of the nozzles, then simulated the injection configuration used in the flight experiment (paper 22 of ref. 8). Six nozzles were made: three with 0.0625-inch-diameter (0.16 cm) orifices and three with 0.125-inch-diameter (0.32 cm) orifices. The orifices were arranged in patterns of 1, 2, or 3 per nozzle as indicated. The spacing between the orifices for the multiple nozzles was in all cases fixed at one orifice diameter. (This spacing was then used in the flight installation.)

A photograph of the plate and nozzle installation is shown in figure 26. A nozzle with 2 orifices of 0.125-inch diameter installed in the test position is shown.

Test Procedure

After the tunnel was started and steady flow conditions were attained, the water was injected in short bursts of approximately 0.3-second duration. The tunnel stagnation pressures and injection pressures were varied during the tests from 100 to 900 psig (689 476 to 6 205 500 N/m) and 50 to 500 psig (344 750 to 3 447 500 N/m), respectively. The maximum penetration of the water spray was determined by illuminating the spray with a light beam through the test-section windows by an arrangement similar to that of figure 4. Motion-picture photography at framing speeds of 200 per second was used to record the penetration. Wall pressures on the mounting plate were monitored during the tests and

UNCLASSIFIED

UNCLASSIFIED

CONFIDENTIAL
APPENDIX

the pressures downstream and to the side of the nozzle (the pressure orifices can be seen in fig. 26) were found to increase with increasing injection rates. The tunnel wall static pressure at a point 11 inches (27.94 cm) upstream of the nozzle was also monitored. When this pressure was affected appreciably by injection, an abrupt change in spray penetration and distribution was observed. This change was attributed to tunnel flow breakdown or choking; hence, no data were used when this forward pressure showed any change due to injection.

Results and Discussion

The results for the maximum cross-current penetration are plotted in figure 27 as the ratio y_{\max}/d_o against the correlating parameter

$$\left(\frac{\rho_l}{\rho_\infty}\right)^{0.36} \left(\frac{V_l}{V_\infty}\right)^{0.819} \left(\frac{x}{d_o}\right)^{0.579}$$

This parameter was found to give the best correlation of all data shown in the figure, including typical data from the scale model tests that are shown for comparison. Note that the exponents on the density and velocity ratios in the correlation parameter are the same as would be obtained from equations (1) and (3). The stream density and velocity for both sets of data were evaluated at free-stream tunnel conditions.

Although there is considerable scatter in these data, the correlation shows that, for the conditions of these tests, the maximum penetration does not depend on the number of orifices at the injection site. That is, the total mass flow is not included in the correlation, but the diameter of the orifices and the density and velocity of the airstream and of the water at the nozzle exit are. It is therefore concluded that the correlations for the Gemini scale models as given by equations (1) to (4) are applicable to a multiple-orifice array, if the d_o is always used directly as the diameter of the orifices.

The correlation also shows that the maximum penetration in the tunnel wall tests with values of d_o up to 0.125 inch (0.32 cm) and where the tunnel wall boundary layer has certainly had some influence can be scaled approximately by the parameters indicated (that is, orifice diameter, free-stream density and velocity, and water exit velocity) and that agreement with the model tests is obtained.

CONFIDENTIAL
UNCLASSIFIED

~~CONFIDENTIAL~~
UNCLASSIFIED

REFERENCES

1. Sisco, W.; and Fiskin, J. M.: Shock Ionization Changes EM Propagation Characteristics. Space/Aeron., vol. 31, no. 3, Mar. 1959, pp. 66-70.
2. Evans, John S.; and Huber, Paul W.: Calculated Radio Attenuation Due to Plasma Sheath on Hypersonic Blunt-Nosed Cone. NASA TN D-2043, 1963.
3. Anon.: Results of the First U.S. Manned Orbital Space Flight February 20, 1962. Manned Spacecraft Center, NASA.
4. Cuddihy, W. F.; and Hughes, J. Kenrick: Simulated Reentry Tests of a Method for Reducing Radio Blackout by Material Addition to Ionized Flow Field. NASA TM X-988, 1964.
5. Cuddihy, William F.; Beckwith, Ivan E.; and Schroeder, Lyle C.: RAM B2 Flight Test of a Method for Reducing Radio Attenuation During Hypersonic Reentry. NASA TM X-902, 1963.
6. Beckwith, Ivan E.; and Huffman, Jarrett K.: Injection and Distribution of Liquids in the Flow Fields of Blunt Shapes at Hypersonic Speeds. NASA TM X-989, 1964.
7. Cuddihy, W. F.; Beckwith, I. E.; and Schroeder, L. C.: A Solution to the Problem of Communications Blackout of Hypersonic Reentry Vehicles. Paper presented at Anti-Missile Research Advisory Council Meeting (Annapolis, Md.), Oct. 1963.
8. Anon.: Conference on Langley Research Related to Apollo Mission. NASA SP-101, 1965.
9. Mechtly, E. A.: The International System of Units - Physical Constants and Conversion Factors. NASA SP-7012, 1964.
10. Stainback, P. Calvin: Heat-Transfer Measurements at a Mach Number of 8 in the Vicinity of a 90° Interior Corner Aligned With the Free-Stream Velocity. NASA TN D-2417, 1964.
11. Lees, Lester, and Reeves, Barry L.: Supersonic Separated and Reattaching Laminar Flows: I. General Theory and Application to Adiabatic Boundary-Layer/Shock-Wave Interactions. AIAA J., vol. 2, no. 11, Nov. 1964, pp. 1907-1920.
12. Zeleznik, Frank J.; and Gordon, Sanford: A General IBM 704 or 7090 Computer Program for Computation of Chemical Equilibrium Compositions, Rocket Performance, and Chapman-Jouguet Detonations. NASA TN D-1454, 1962.
13. Price, Earl A.; Stallings, Robert L., Jr.; and Howard, Paul W.: Pressure and Heat-Transfer Distributions of 0.1-Scale Gemini Exit and Reentry Models at Mach Numbers of 3.51 and 4.44. NASA TM 1149, 1965.

~~CONFIDENTIAL~~
UNCLASSIFIED

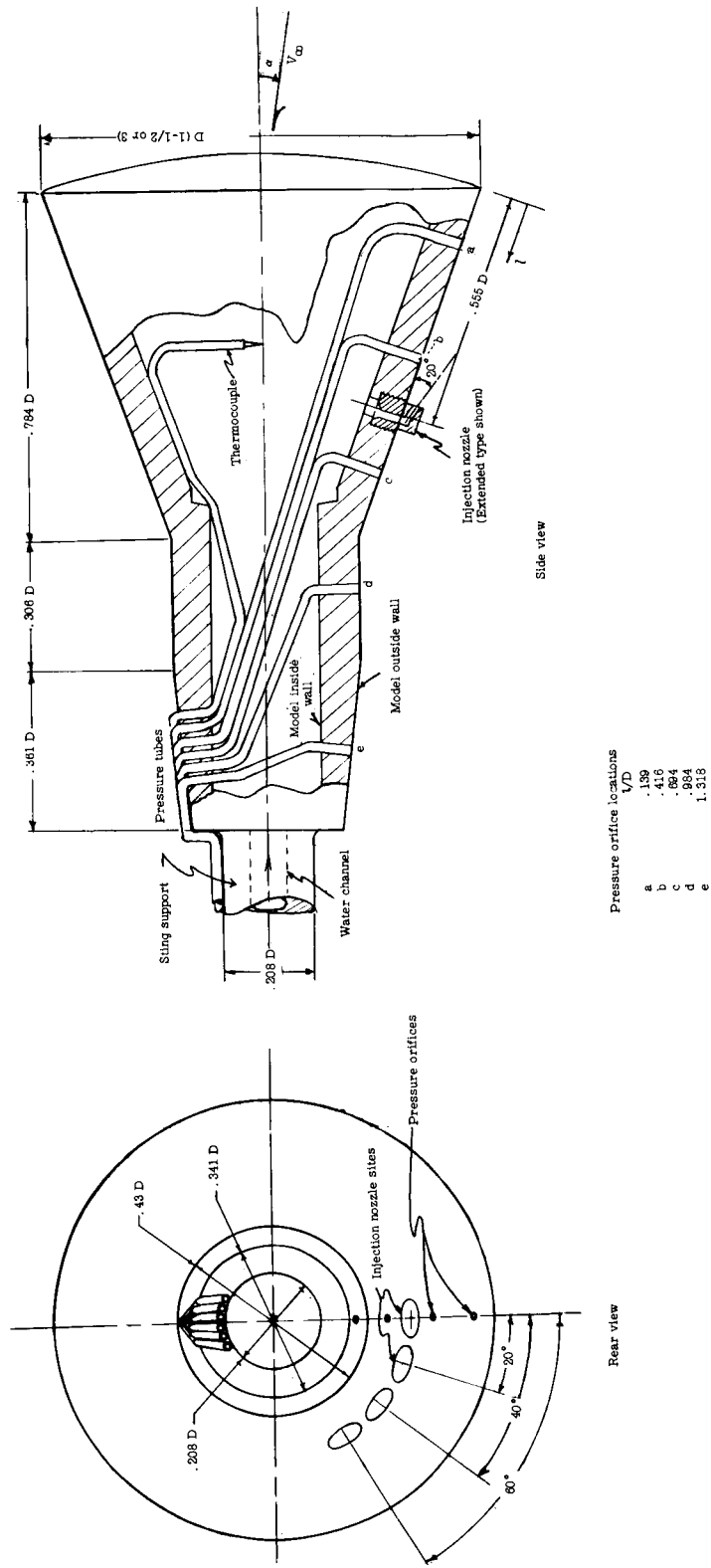
UNCLASSIFIED

~~CONFIDENTIAL~~

14. Marshall, L. A.; and Giragosian, P. A.: Hypersonic Aerodynamic Characteristics of Blunt Faced Lifting Reentry Vehicles. Paper No. 62-169, Inst. Aerospace Sci., June 1962.
15. Ingebo, Robert D.; and Foster, Hampton H.: Drop-Size Distribution for Crosscurrent Breakup of Liquid Jets in Airstreams. NACA TN 4087, 1957.
16. Beckwith, Ivan E.; and Bushnell, Dennis M.: Effect of Intermittent Water Injection on Aerodynamic Heating of a Sphere-Cone at Flight Velocities to 18 000 Feet Per Second. NASA TM X-1128, 1965.
17. Kruse, Robert L.; Malcolm, Gerald N.; and Short, Barbara J.: Comparison of Free-Flight Measurements of Stability of the Gemini and Mercury Entry Capsules at Mach Numbers 3 and 9.5. NASA TM X-957, 1964.

~~CONFIDENTIAL~~

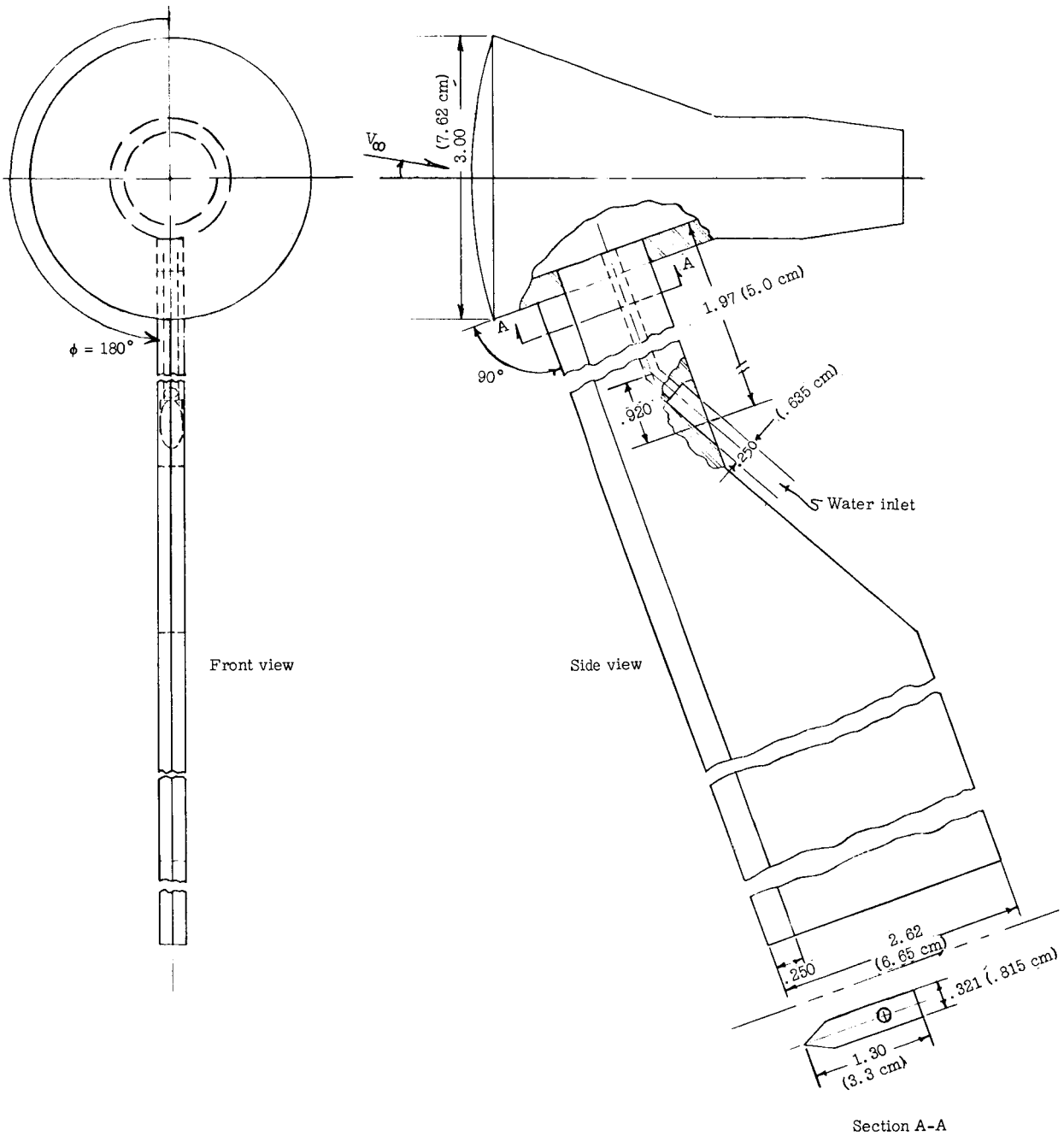
UNCLASSIFIED



(a) Pressure orifice and injection nozzle installation on 1/30- and 1/60-scale models with rear sting.

Figure 1.- Cutaway view of models.

UNCLASSIFIED



(b) 1/30-scale model with side support strut. Injection nozzles are on opposite side from support strut at values of ϕ shown in figure 10.

Figure 1.- Concluded.

UNCLASSIFIED

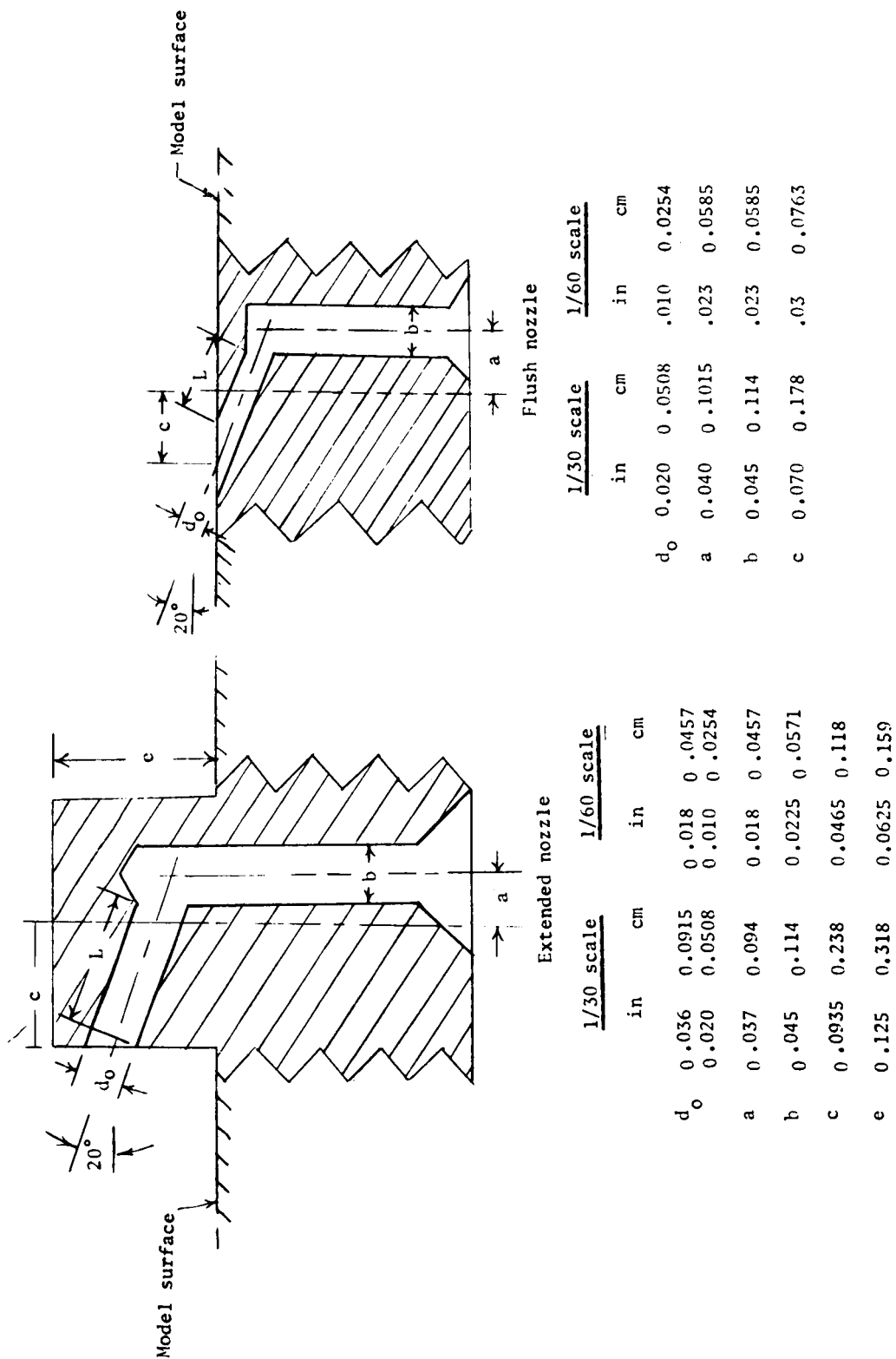


Figure 2.- Sketch of injection nozzles used on Gemini scale models. $L/d_o \geq 3$.

UNCLASSIFIED

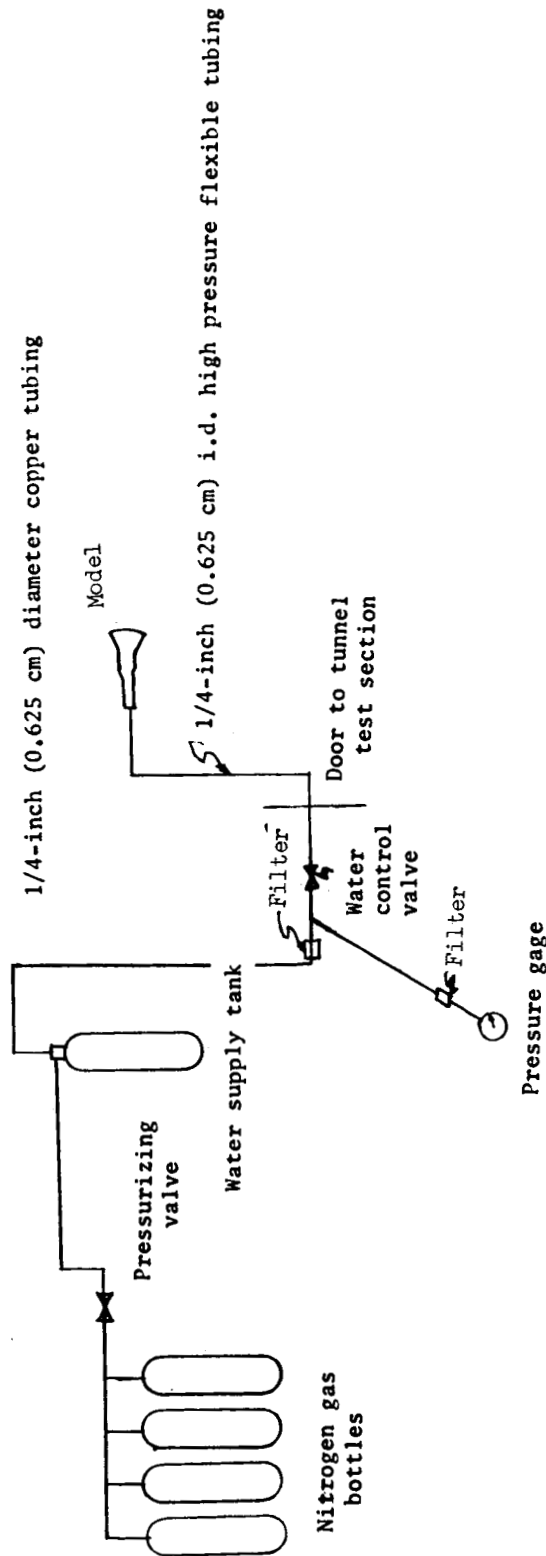


Figure 3.- Schematic diagram of water supply system.

UNCLASSIFIED

UNCLASSIFIED

Type of support	β , deg	θ , deg	g in.	h in.	h cm	i in.	i cm
Rear sting	16°	14.4°	22.25	0	0	-1	-2.5
Side strut	-38.6°	-7.3°	30	4	10	3.23	8.08

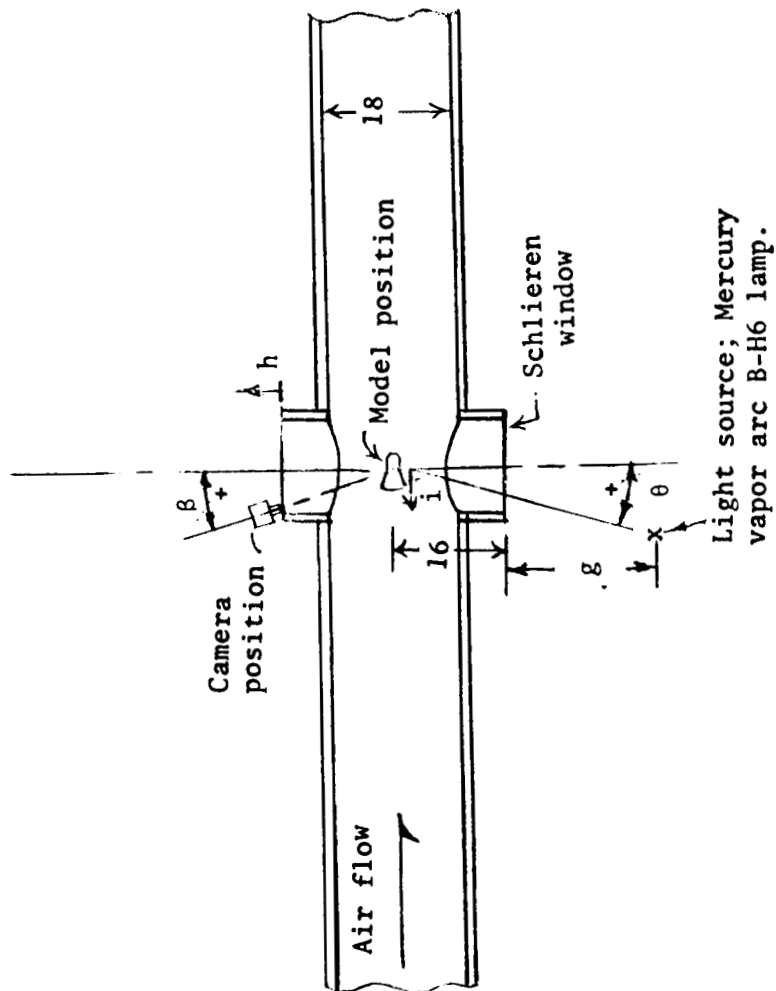
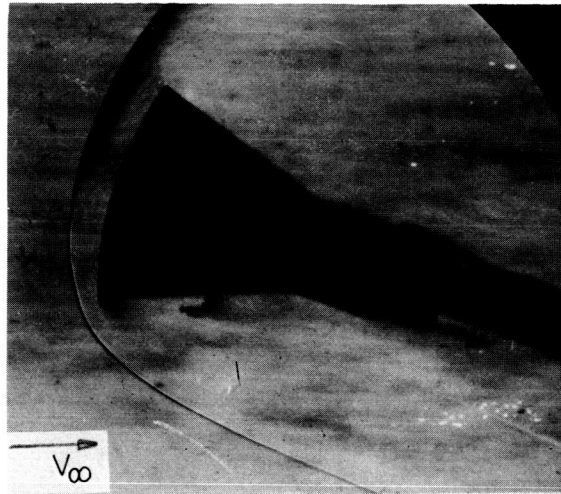


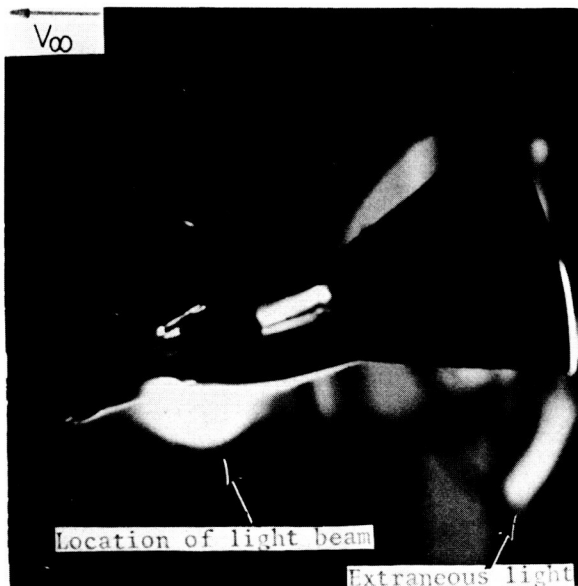
Figure 4.- Schematic top view of wind tunnel showing approximate location of light source and camera used to record liquid spray distribution for both side and rear sting models.

UNCLASSIFIED

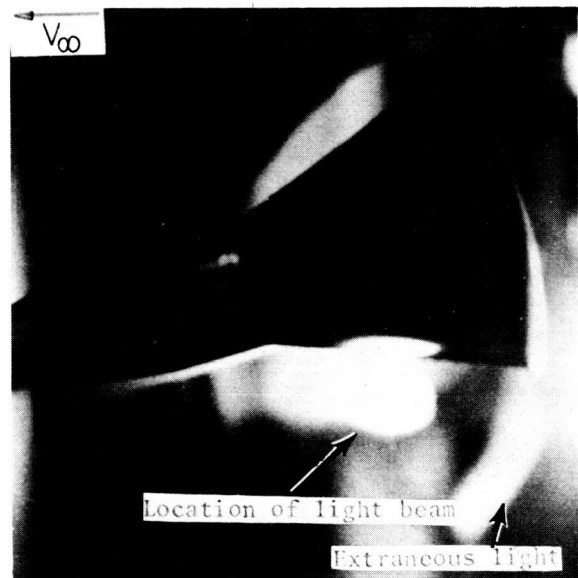
UNCLASSIFIED



Schlieren of flow field



Penetration at $x/D \approx 1$



Penetration at $x/D \approx 0$

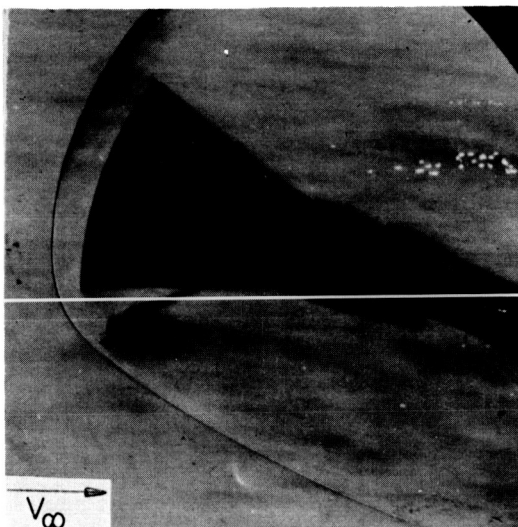
(a) $\bar{V} = 344$; $\bar{W} = 0.0153$; $\bar{M} = 0.00021$.

L-65-7952

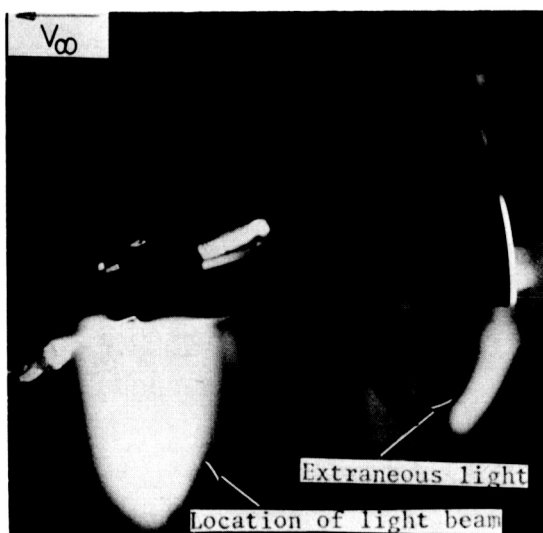
Figure 5.- Schlieren and penetration photographs of the 1/30-scale model rear sting supported with $d_o = 0.020$ -inch-diameter (0.050 cm) flush nozzle. Arrows indicate direction of air flow.

UNCLASSIFIED

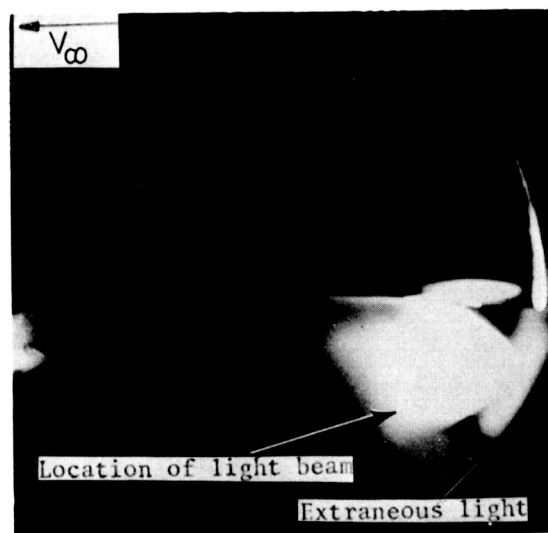
UNCLASSIFIED



Schlieren of flow field



Penetration at $x/D \approx 1$



Penetration at $x/D \approx 0$

(b) $\bar{V} = 1367$; $\bar{W} = 0.0607$; $\bar{M} = 0.00192$.

L-65-7953

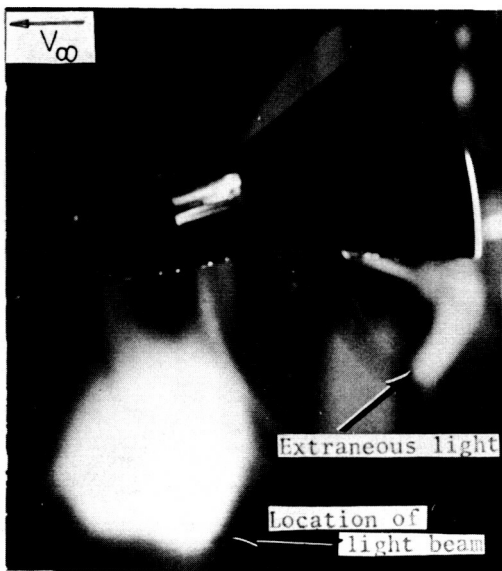
Figure 5.- Continued.

UNCLASSIFIED

UNCLASSIFIED



Schlieren of flow field.



Penetration at $x/D \approx 1$



Penetration at $x/D \approx 0$

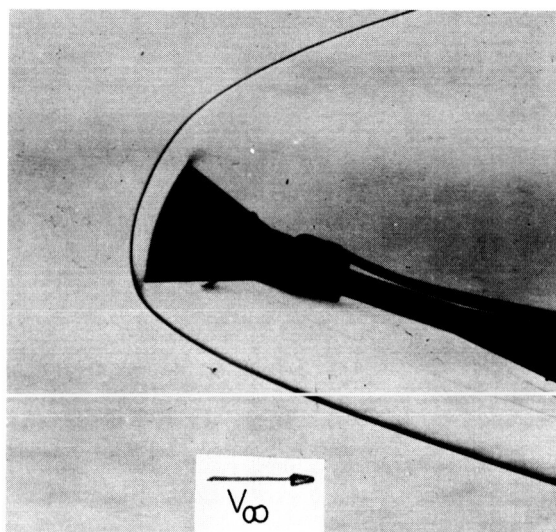
(c) $\bar{V} = 6498$; $\bar{W} = 0.2887$; $\bar{M} = 0.0123$.

L-65-7954

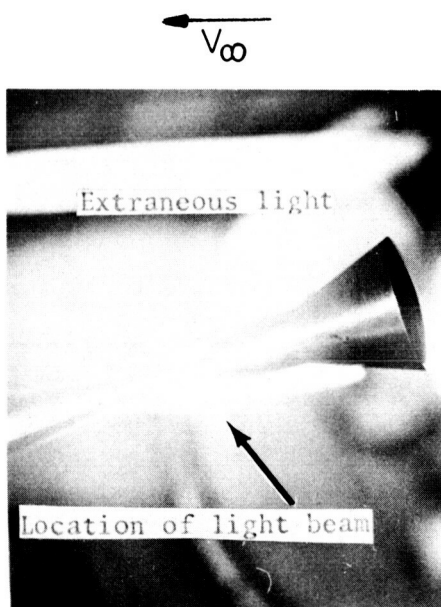
Figure 5.- Concluded.

UNCLASSIFIED

UNCLASSIFIED



Schlieren of flow field



Penetration at $x/D \approx 1$



Penetration at $x/D \approx 0$

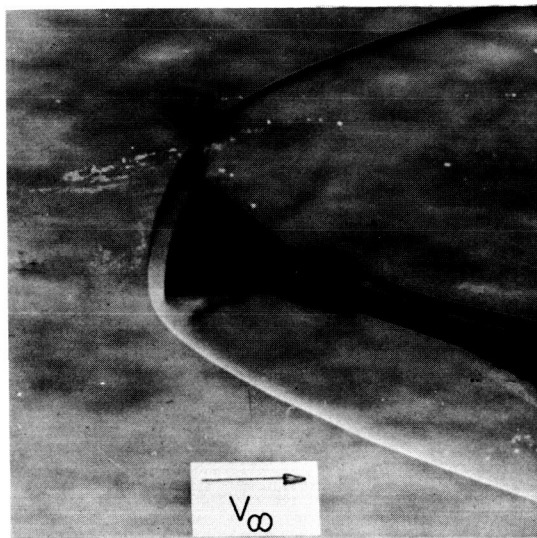
(a) $\bar{V} = 271$; $\bar{W} = 0.0170$; $\bar{M} = 0.00034$; flush nozzle.

L-65-7955

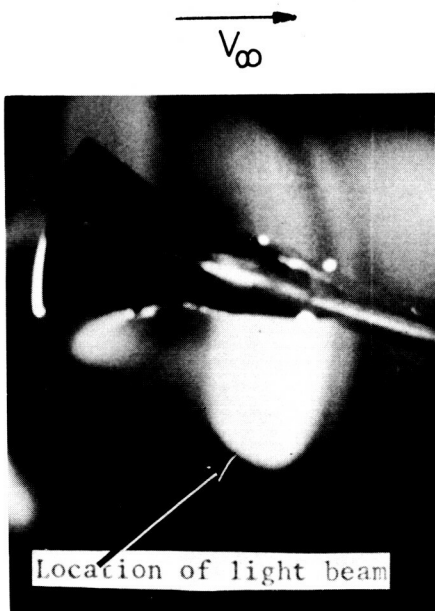
Figure 6.- Schlieren and penetration photographs of the 1/60-scale Gemini rear sting model with $d_o = 0.010$ -inch-diameter (0.025 cm) nozzle. Arrows indicate direction of air flow.

UNCLASSIFIED

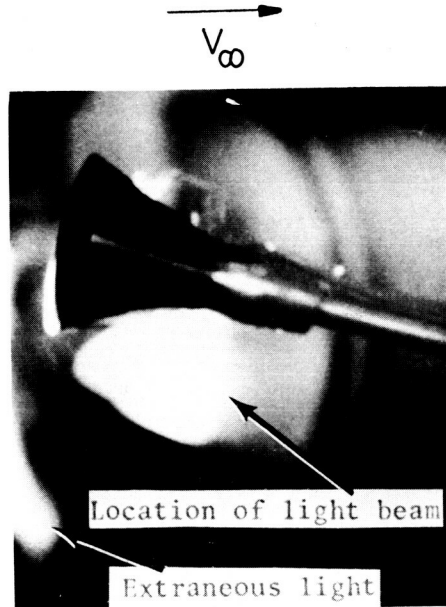
UNCLASSIFIED



Schlieren of flow field



Penetration at $x/D \approx 1$



Penetration at $x/D \approx 0$

(b) $\bar{V} = 1355$; $\bar{W} = 0.0602$; $\bar{M} = 0.00195$; extended nozzle. L-65-7956

Figure 6.- Concluded.

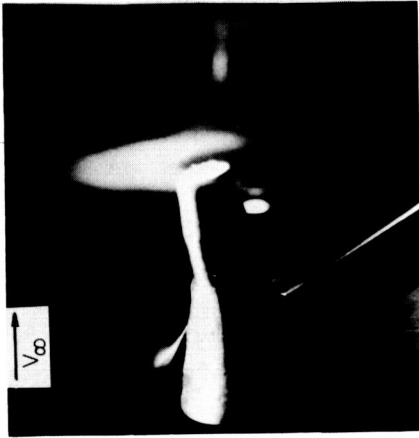
UNCLASSIFIED



$x/D \approx 1.35$

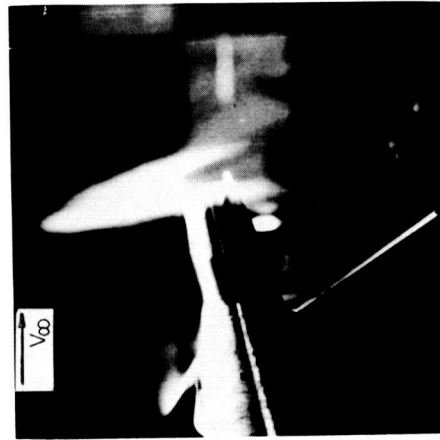


$x/D \approx 1.35$



$x/D \approx 1$

(a) Injection orifice at $\phi = 0$; $\bar{V} = 1200$; $\bar{w} = 0.055$; $\bar{M} = 0.0016$.



$x/D \approx 1$



$x/D \approx 0$



$x/D \approx 0$

(b) Injection orifice at $\phi = 20^\circ$; $\bar{V} = 940$; $\bar{w} = 0.042$; $\bar{M} = 0.00156$.

Figure 7.- Photographs of spray at different downstream stations for strut supported 1/30-scale model. $\alpha = 15^\circ$; 0.020-inch-diameter (0.050 cm) flush-mounted nozzle. L-65-7957

UNCLASSIFIED

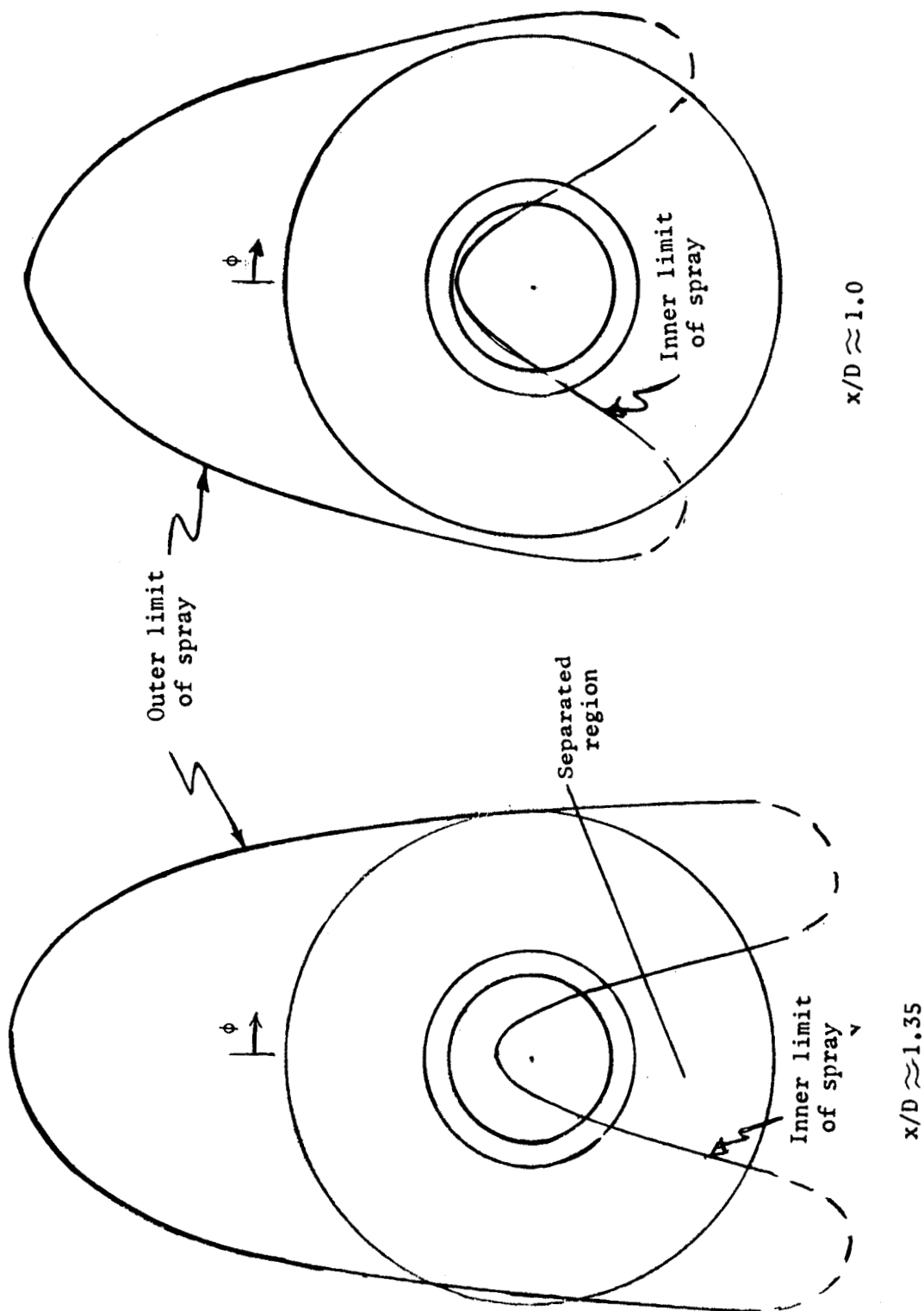


Figure 8.- Typical spray cross sections as viewed from the rear for the strut-supported 1/30-scale model. Same injection conditions as those of figure 7(a).

UNCLASSIFIED

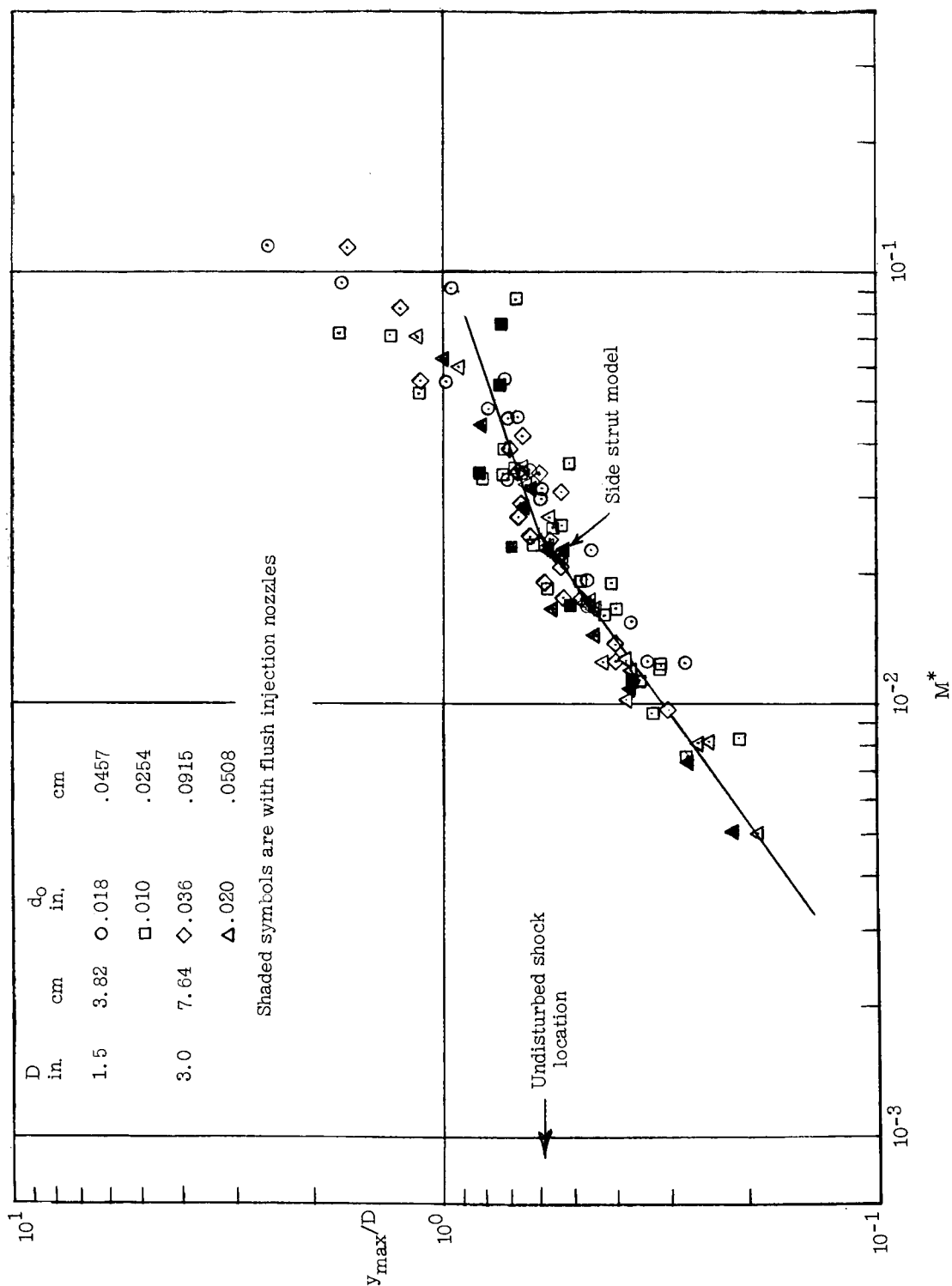


Figure 9.- Correlation of maximum cross-stream penetration of liquid spray. All data are from the rear-sting-supported model except as indicated.

UNCLASSIFIED

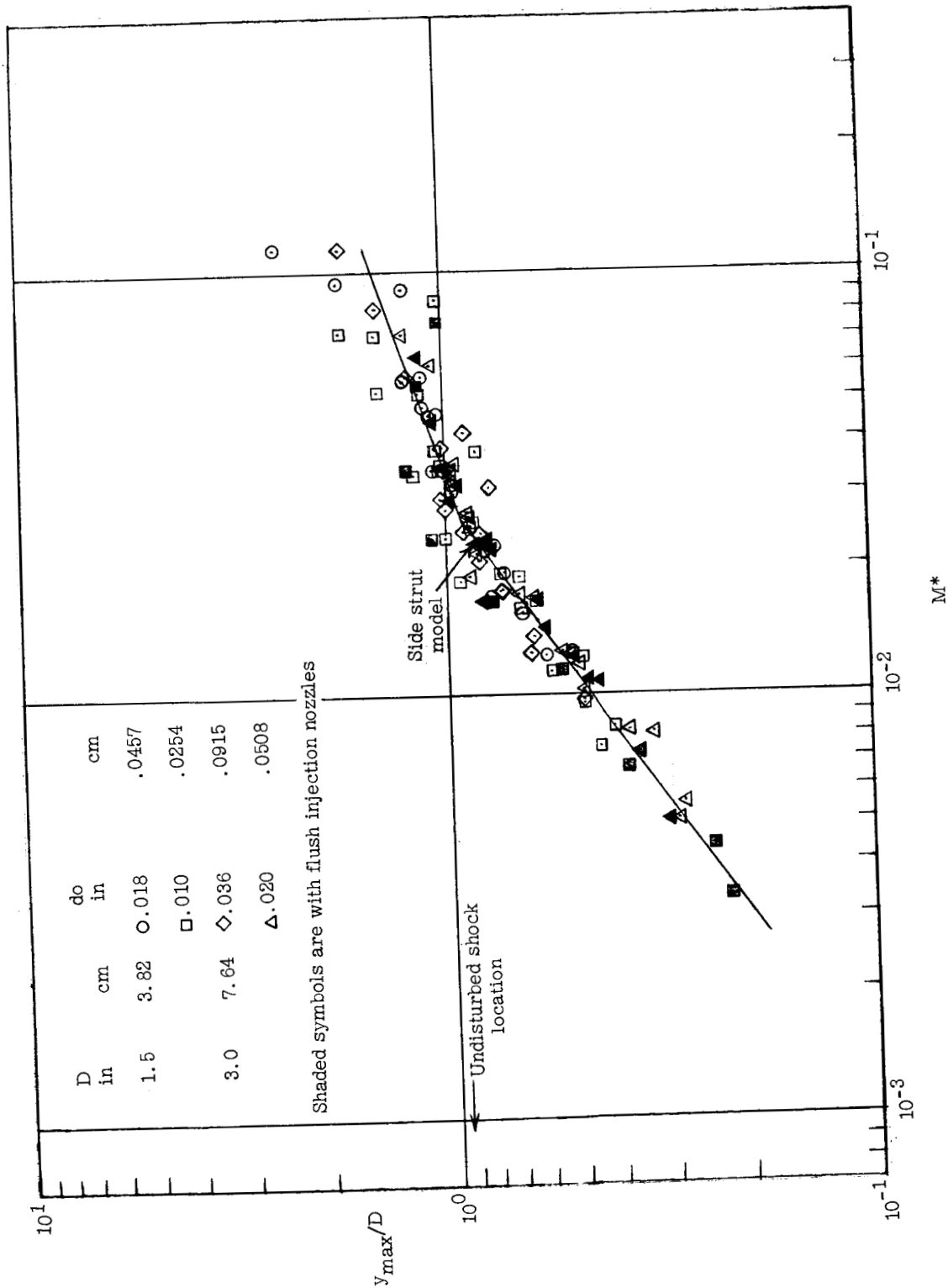


Figure 9.- Concluded.

UNCLASSIFIED

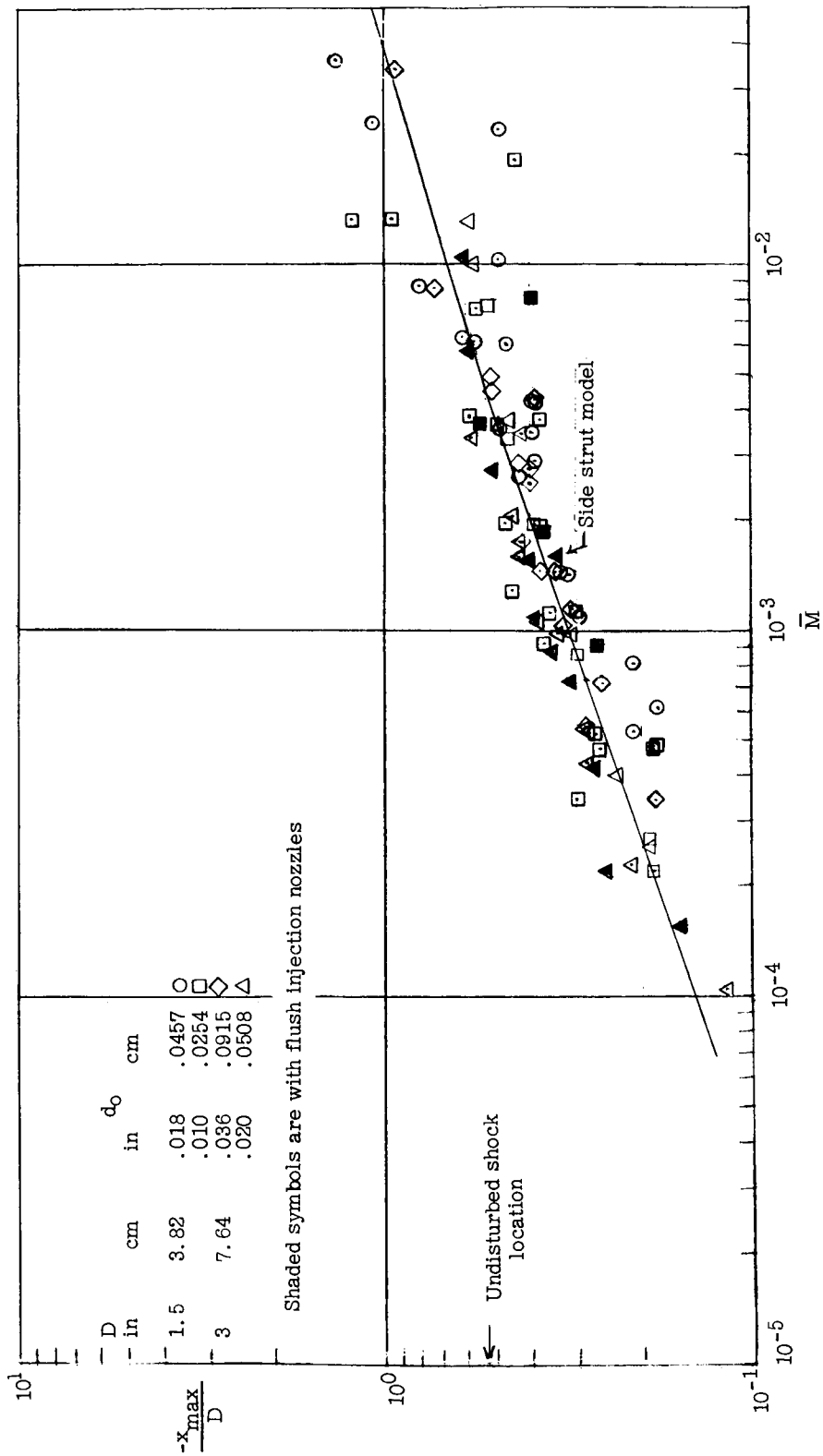
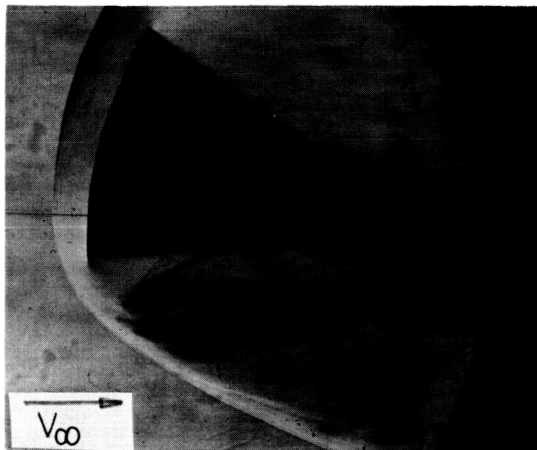
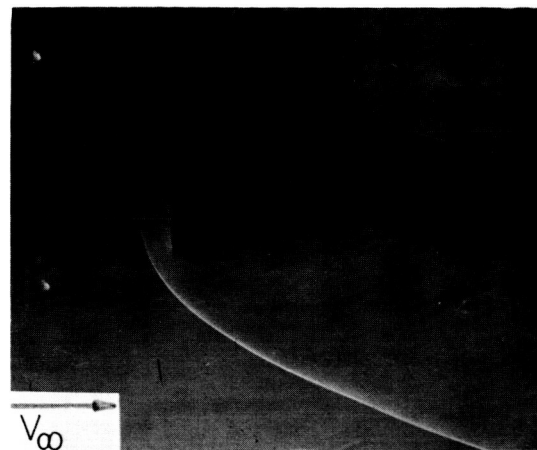


Figure 10.- Correlation of maximum forward penetration of the liquid spray. All data are from the rear-sting-supported model except as indicated.

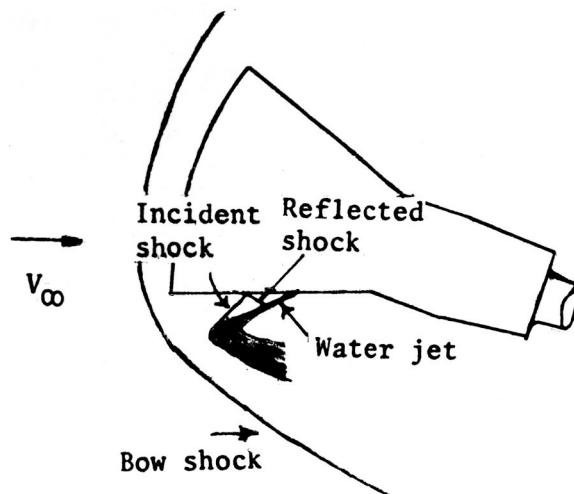
UNCLASSIFIED



(a) Injection with $\bar{M} = 1.62 \times 10^{-3}$.



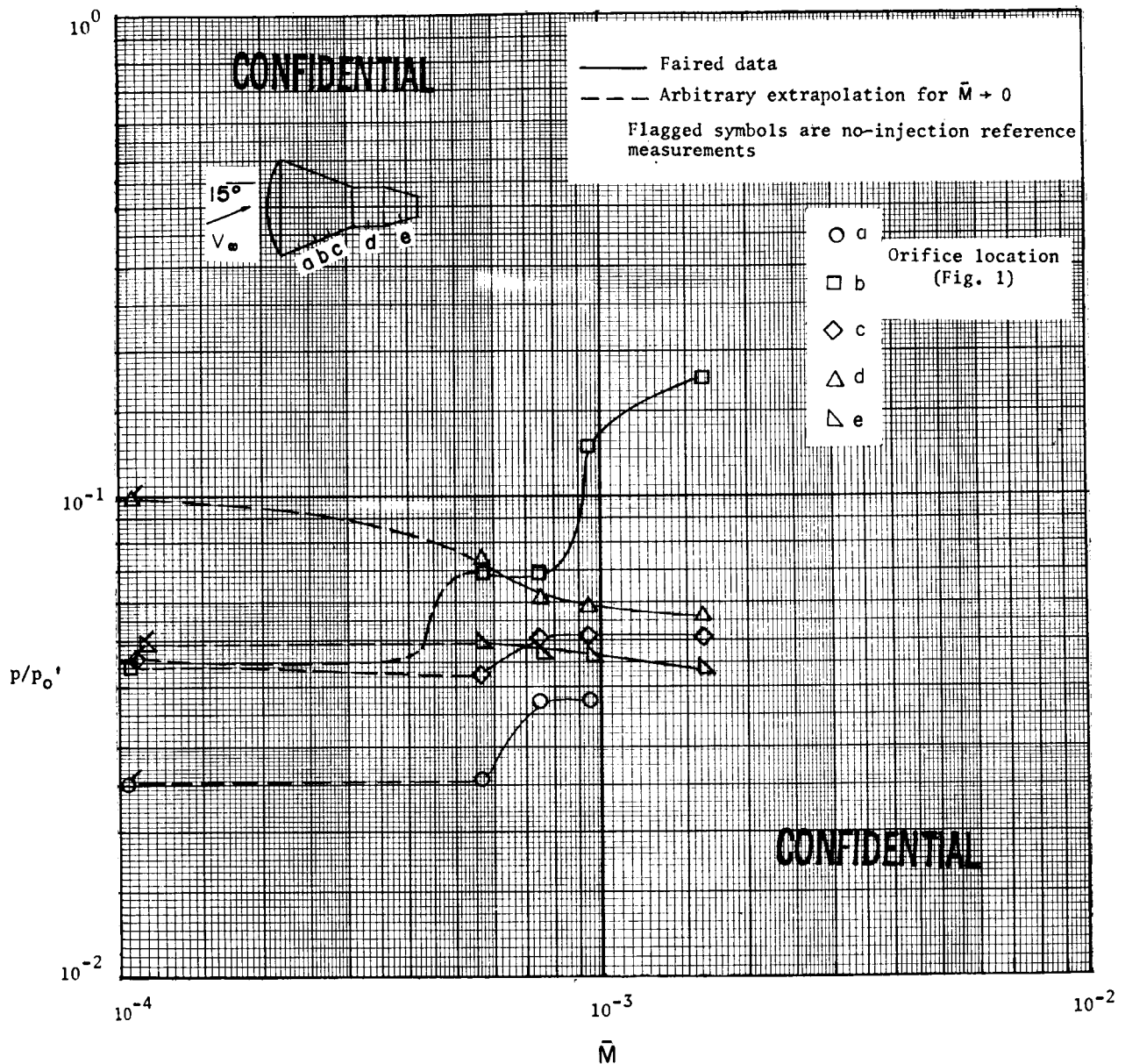
(b) No injection. L-65-7958



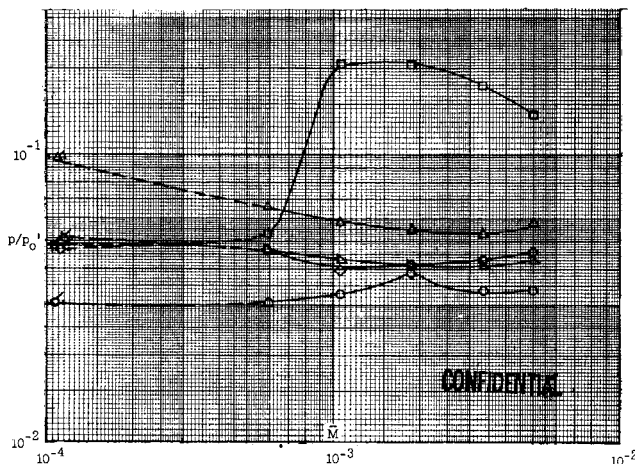
(c) Schematic of injection case.

Figure 11.- Schlieren of the flow field showing secondary shock system caused by water jet. Rear-sting-supported 1/30-scale model at $\alpha = 15^\circ$ with 0.020-inch-diameter (0.050 cm) flush nozzle.

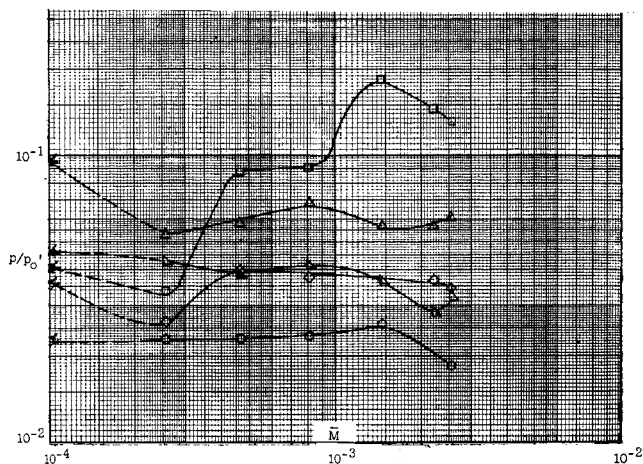
UNCLASSIFIED



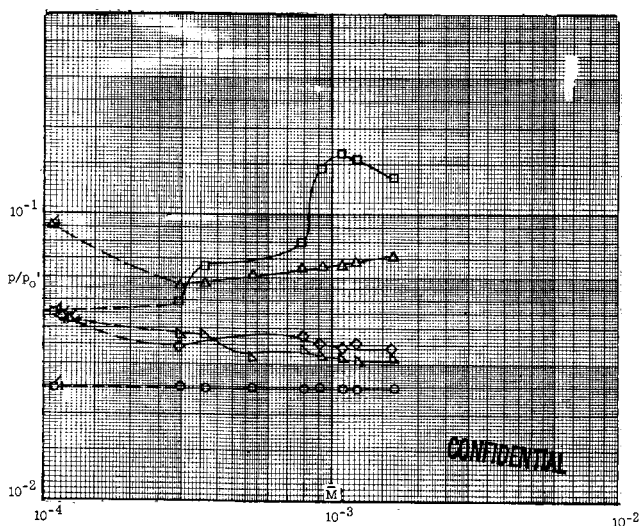
UNCLASSIFIED



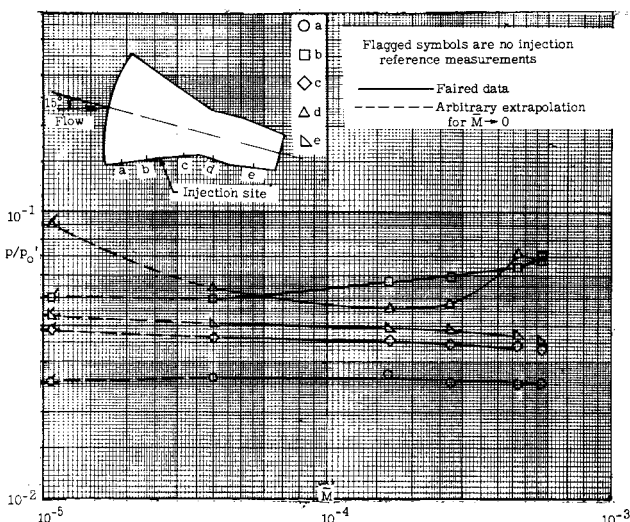
(a) $R_{\infty,D} = 4.18 \times 10^5$.



(b) $R_{\infty,D} = 7.15 \times 10^5$.



(c) $R_{\infty,D} = 10.65 \times 10^5$.



(d) $R_{\infty,D} = 25.5 \times 10^{-5}$.

Figure 13.- Effect of injection on pressure ratio along the windward ray. Rear-sting-supported 1/30-scale model; 0.020-inch-diameter (0.050 cm) flush nozzle.

UNCLASSIFIED

UNCLASSIFIED

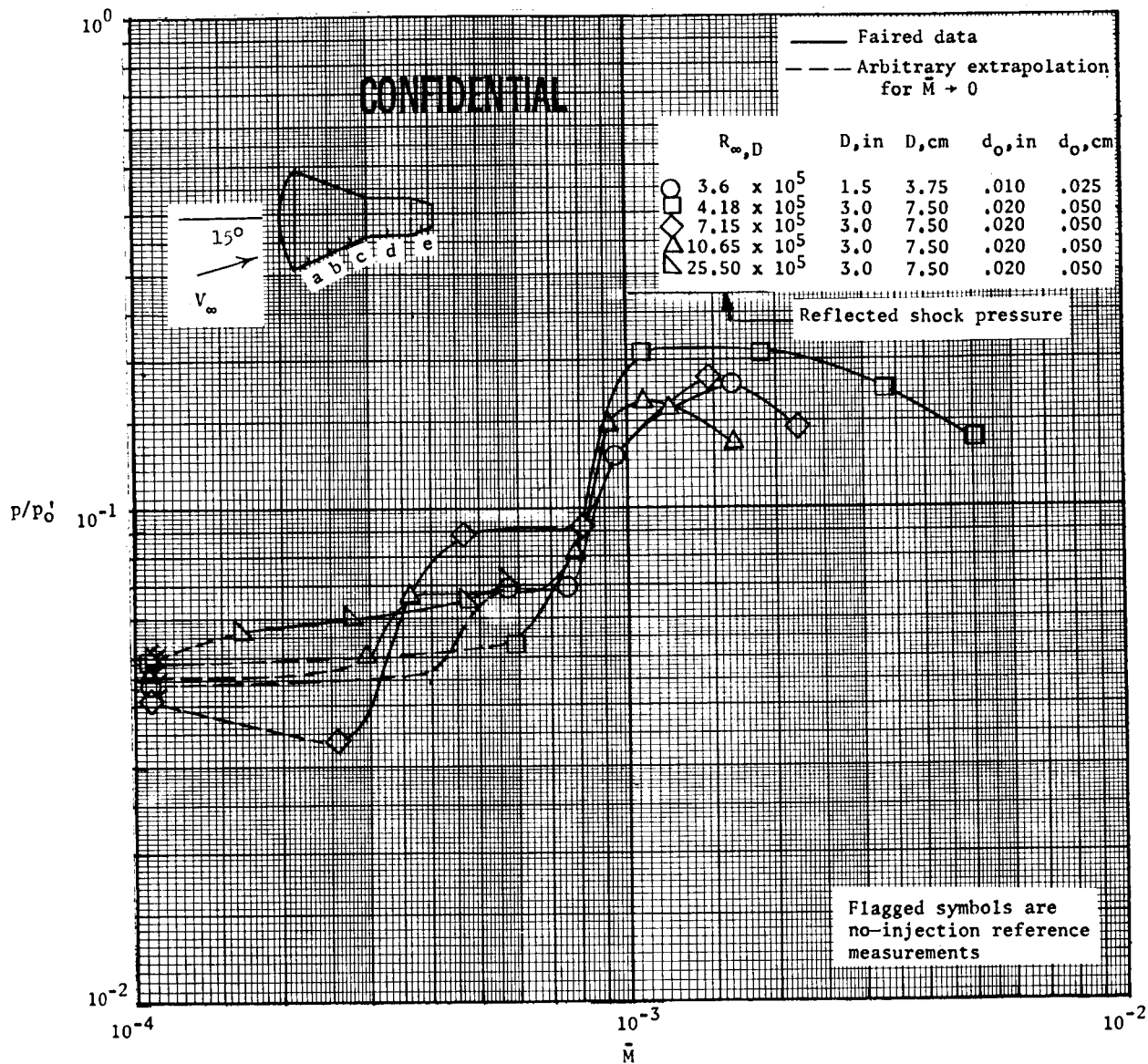
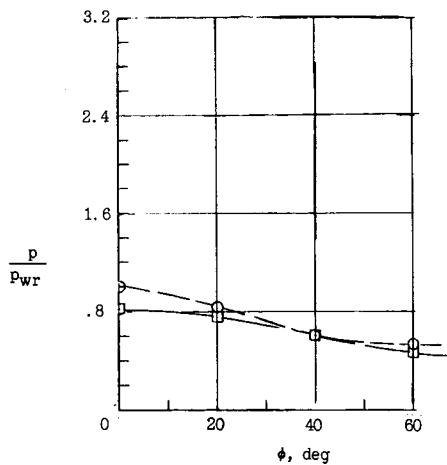


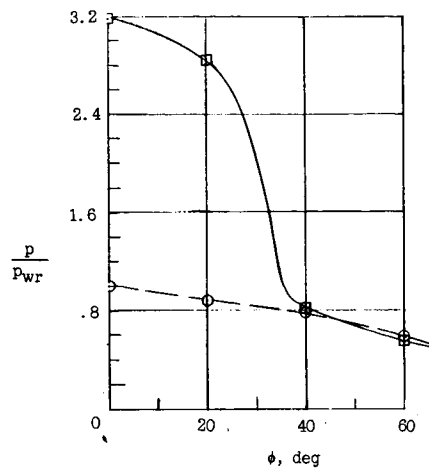
Figure 14.- Effect of injection on pressure ratio at orifice location b for the Reynolds number range of the tests. Data from figures 12 and 13.

~~CONFIDENTIAL~~
UNCLASSIFIED

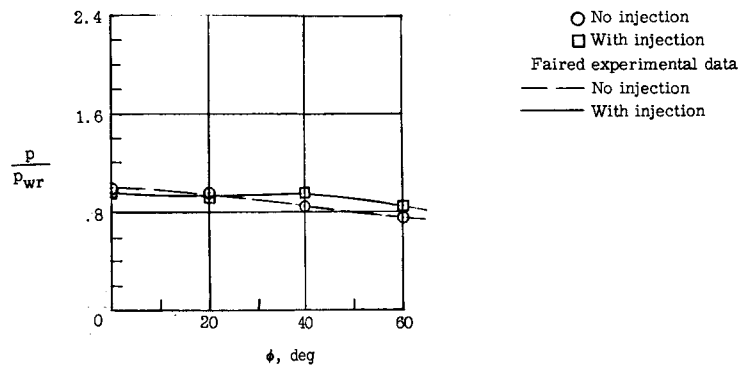
UNCLASSIFIED



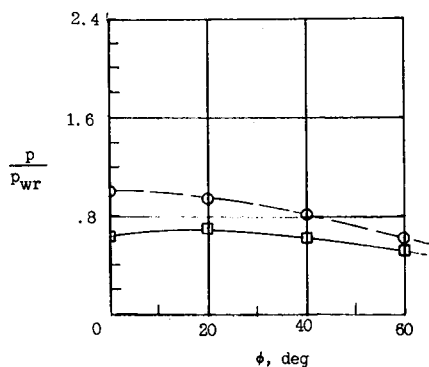
(a) Station a.



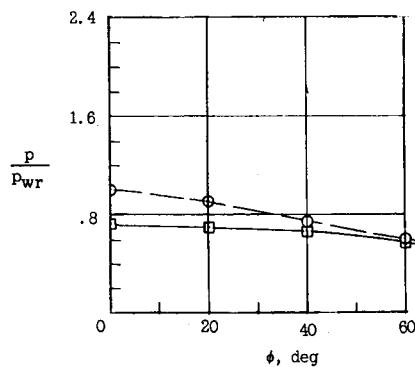
(b) Station b.



(c) Station c.



(d) Station d.



(e) Station e.

Figure 15.- Effect of injection on the lateral pressure distribution. Injection nozzle at windward ray ($\phi = 0^\circ$); rear-sting-supported 1/30-scale model; $R_{w,D} = 7.15 \times 10^5$; $\bar{M} = 2.55 \times 10^{-3}$; $d_o = 0.02$ -inch (0.05 cm) flush nozzle.

UNCLASSIFIED

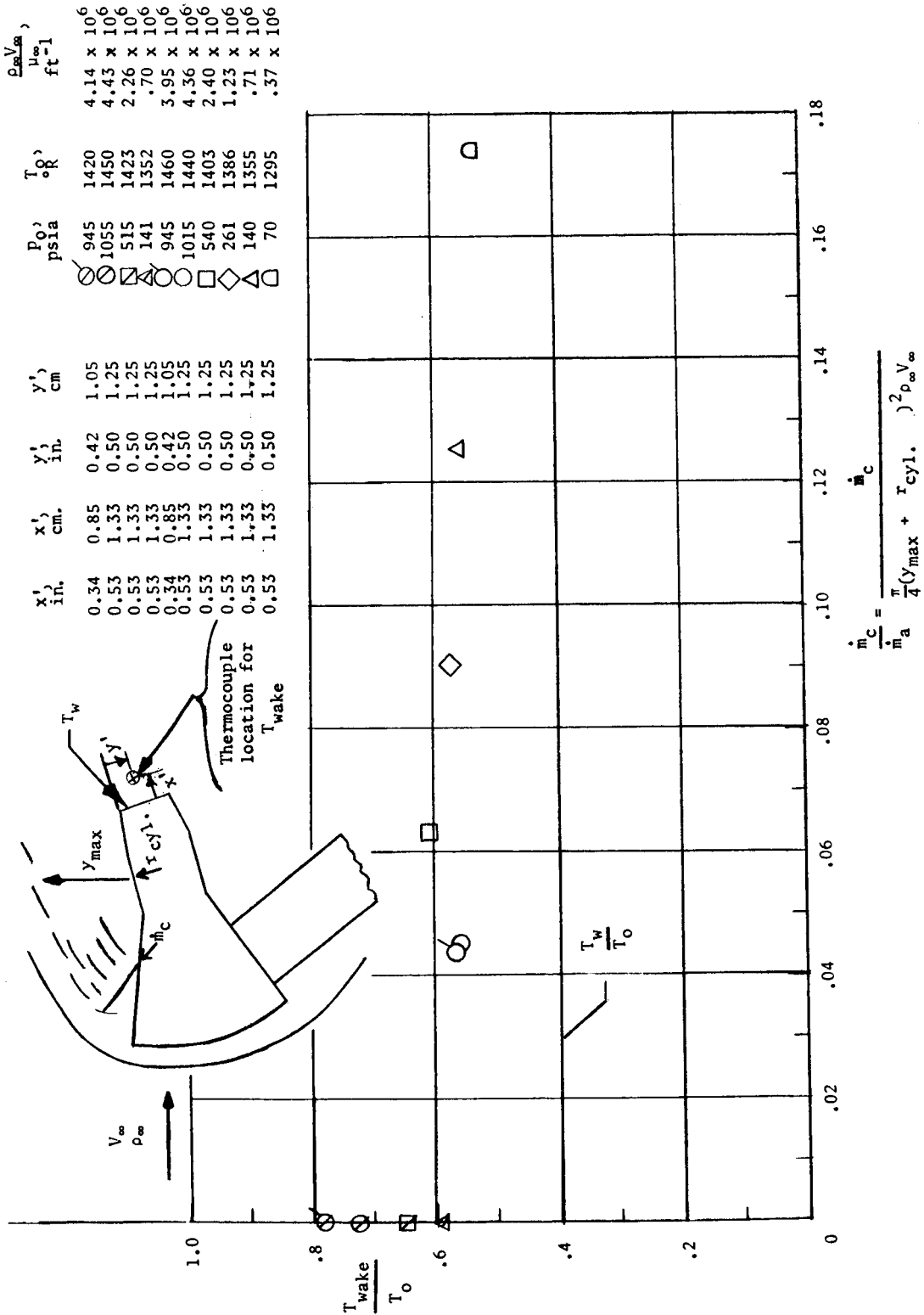
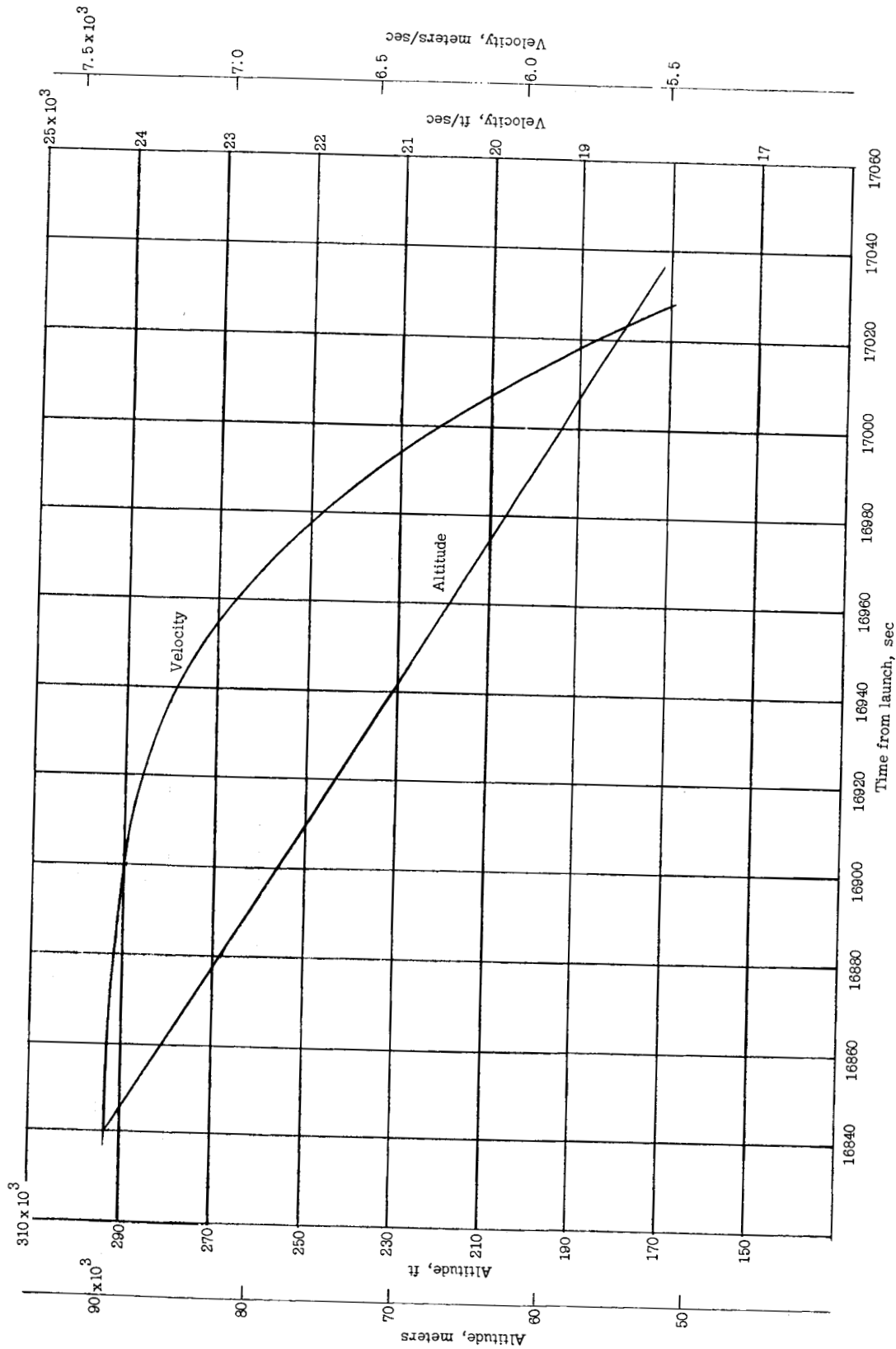


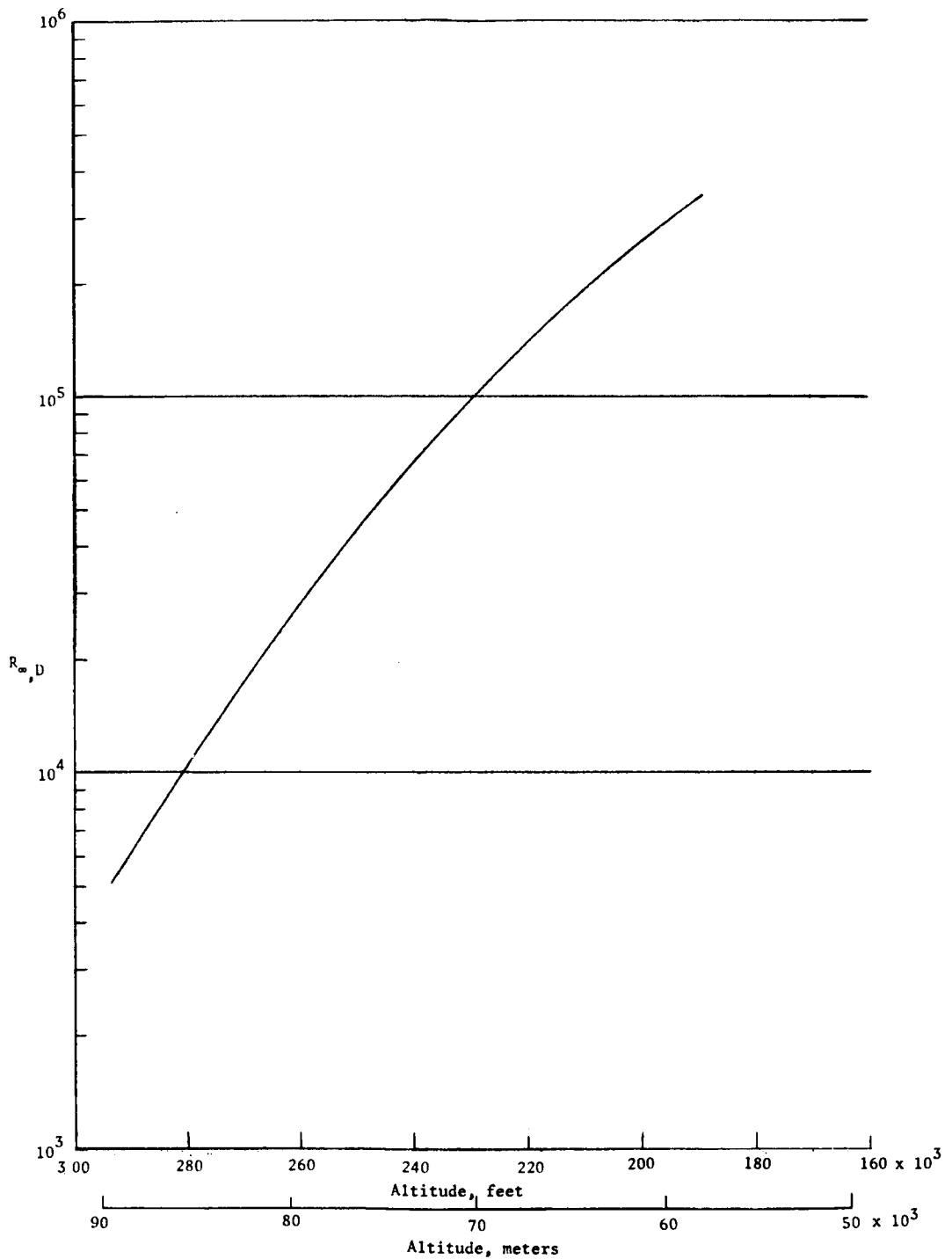
Figure 16.- Effect of injection on temperature in near wake. Side-strut supported, 1/30-scale model at $\alpha = 15^\circ$ with $d_o = 0.02$ -inch (0.05 cm) flush nozzle.

UNCLASSIFIED



(a) Variation of altitude and velocity with time.
Figure 17.- Trajectory parameters for GT-3 reentry.

UNCLASSIFIED



(b) $R_{\infty, D}$ variation with altitude.

Figure 17.- Concluded.

UNCLASSIFIED

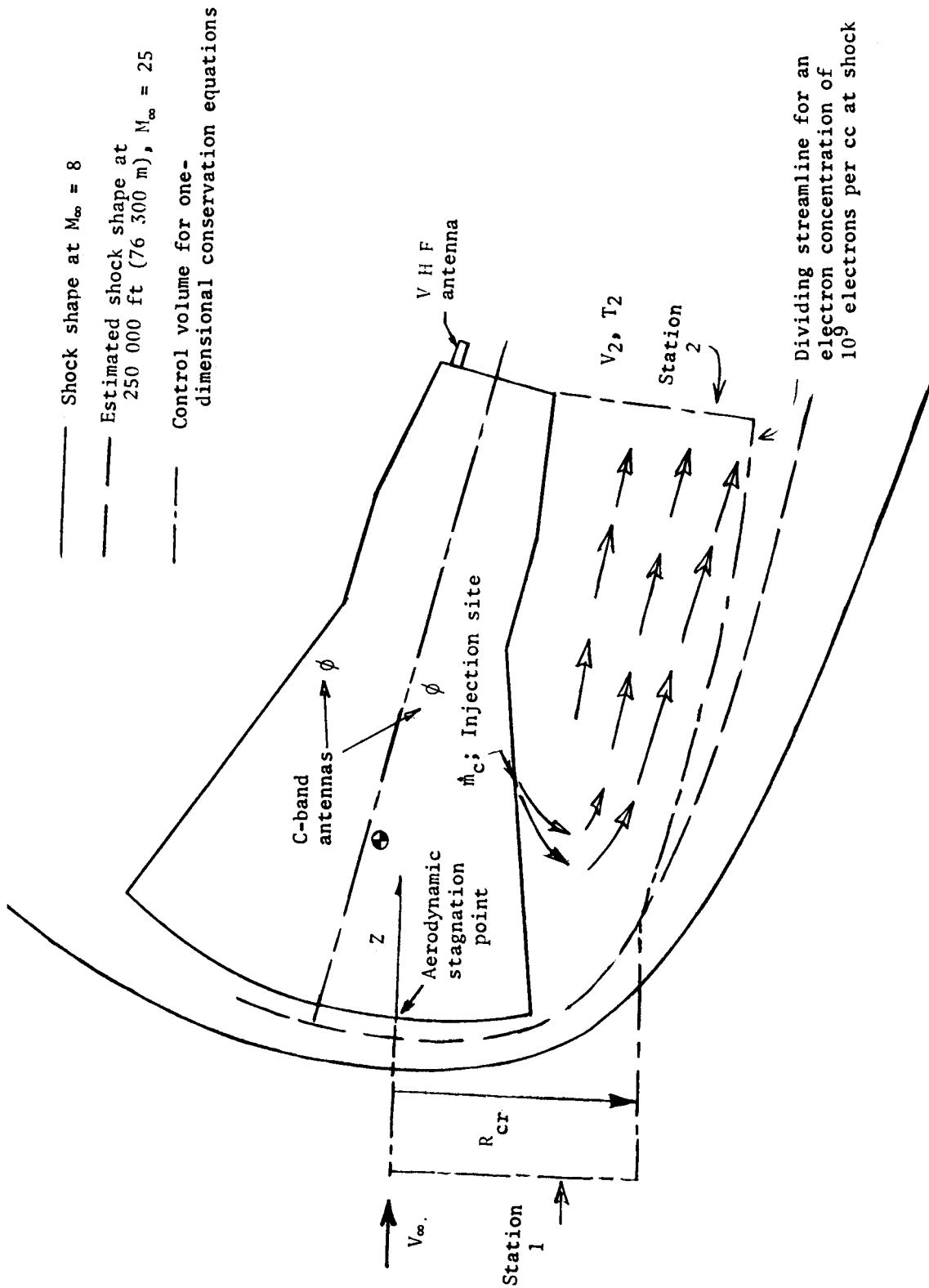


Figure 18.- Sketch of flow field and control volume used to estimate water flow rate requirements for Gemini reentry. $\alpha = 15^\circ$.

UNCLASSIFIED

UNCLASSIFIED

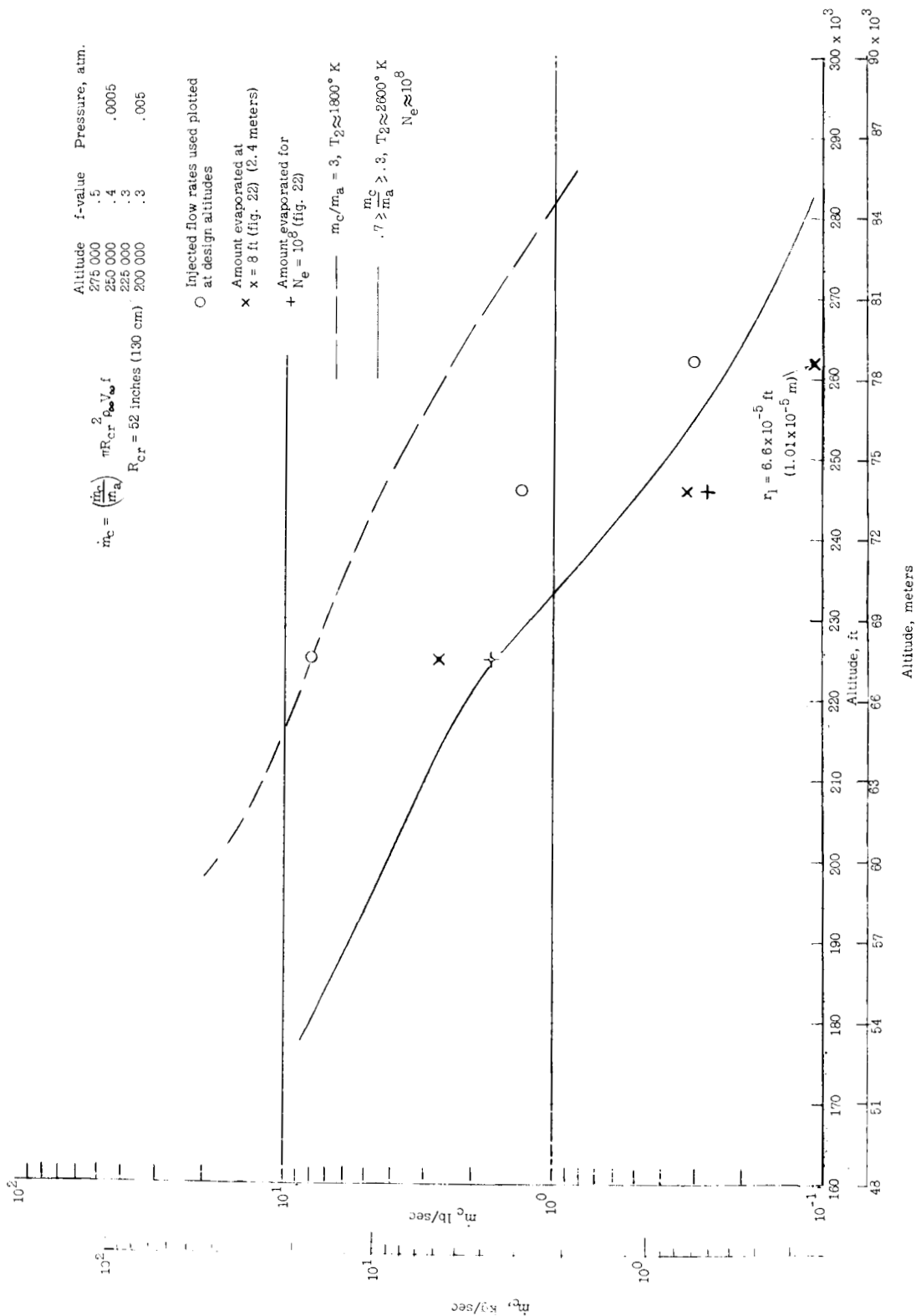
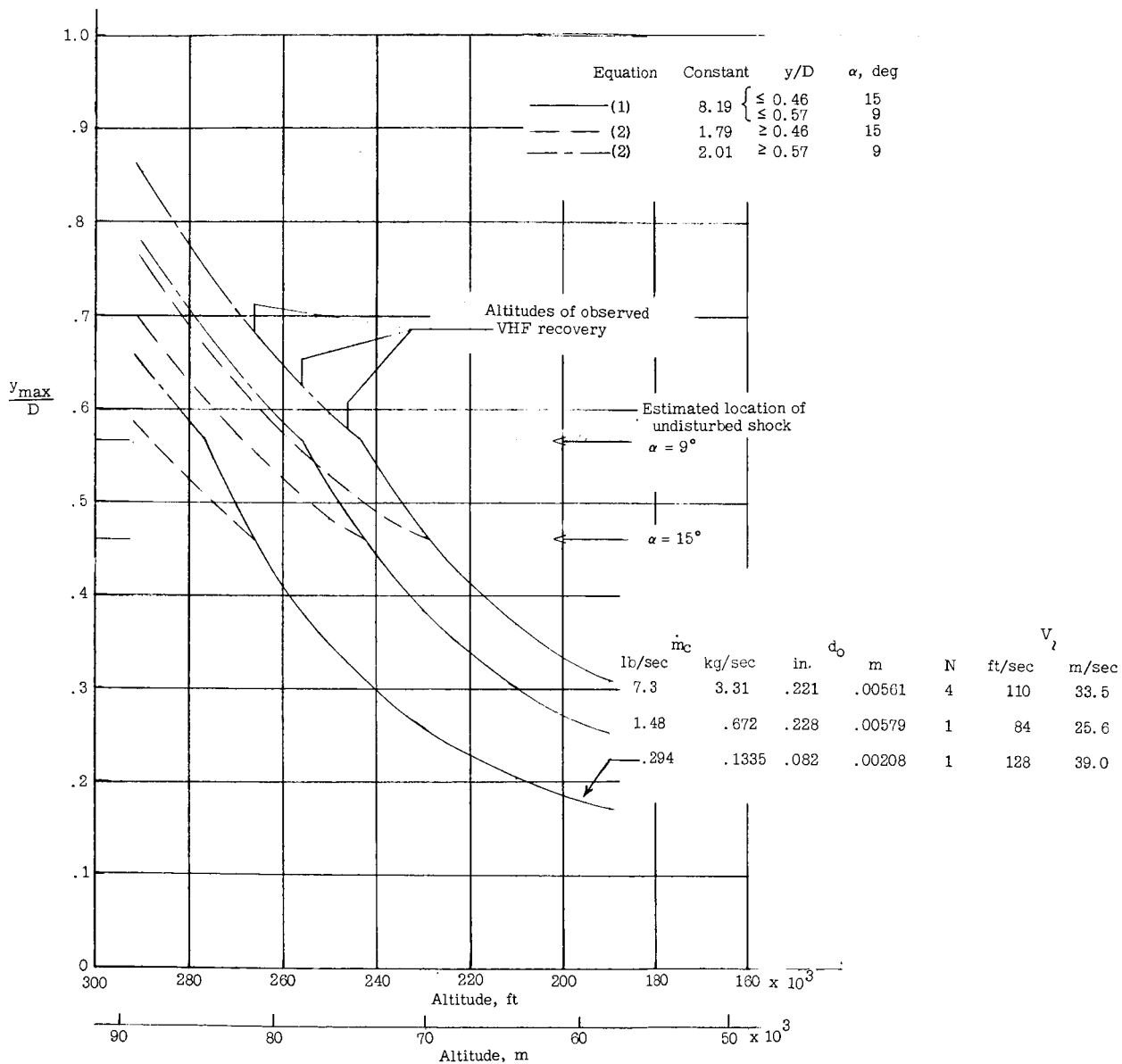


Figure 19.- Estimated injection flow rates for Gemini reentry based on one-dimensional conservation equations and equilibrium chemistry. $\alpha = 15^\circ$; injection from windward side.

UNCLASSIFIED

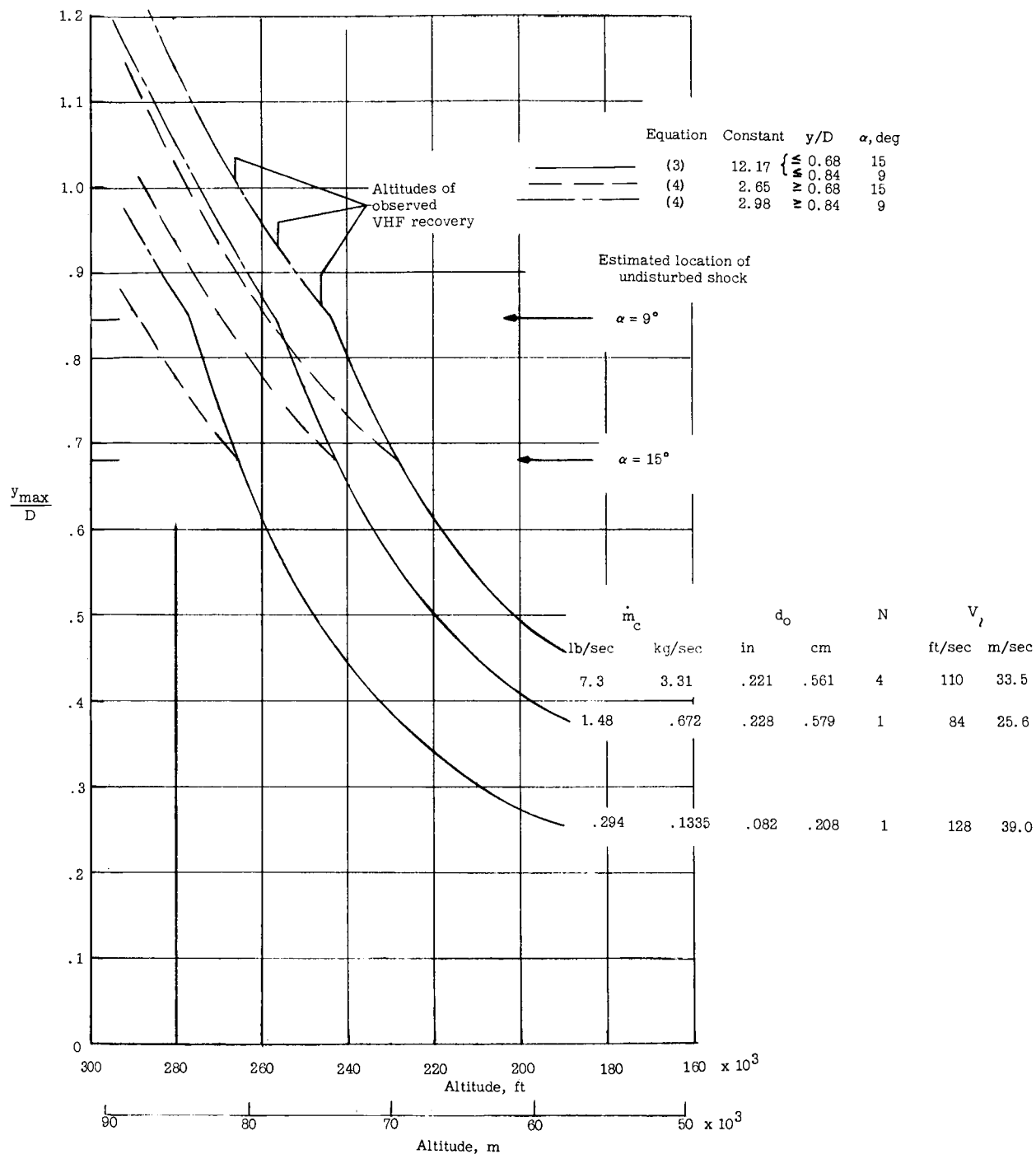
UNCLASSIFIED



(a) $\frac{x}{D} = 0$.

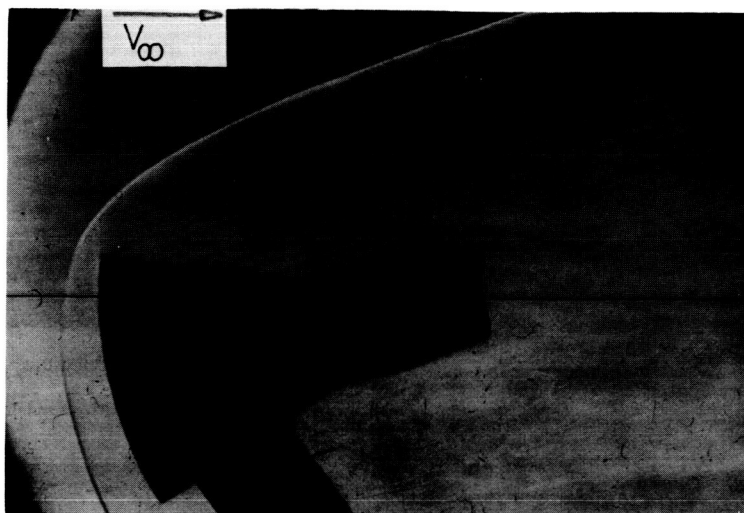
Figure 20.- Predicted spray penetration for the Gemini reentry communications experiment.

UNCLASSIFIED

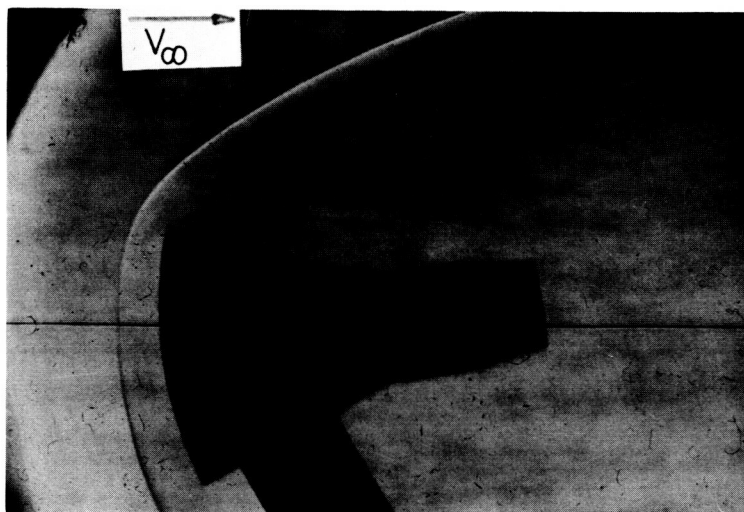


(b) $\frac{x}{D} = 1.0$.

Figure 20.- Concluded.



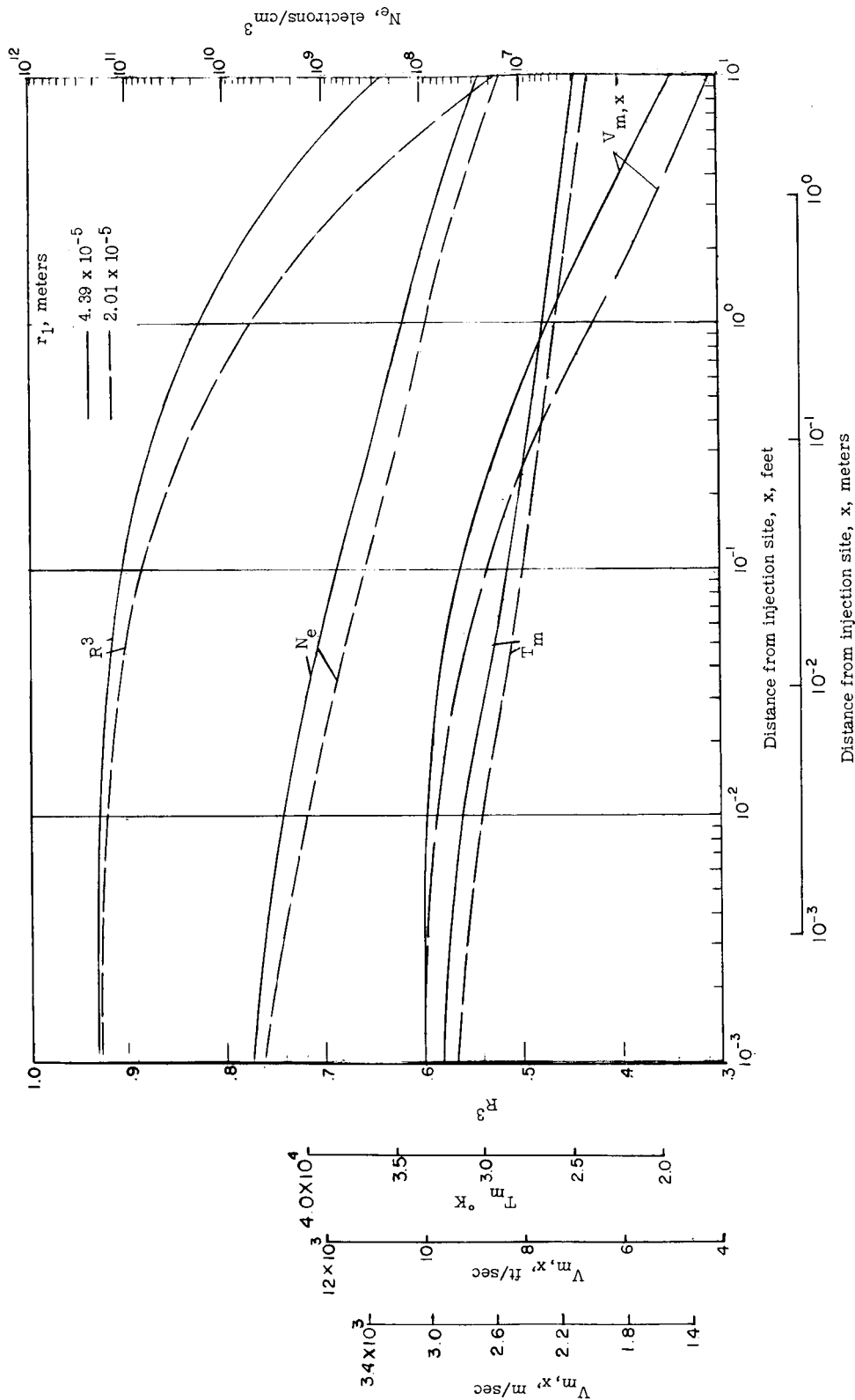
$\alpha = 15^\circ$



$\alpha = 9^\circ$

L-65-7959

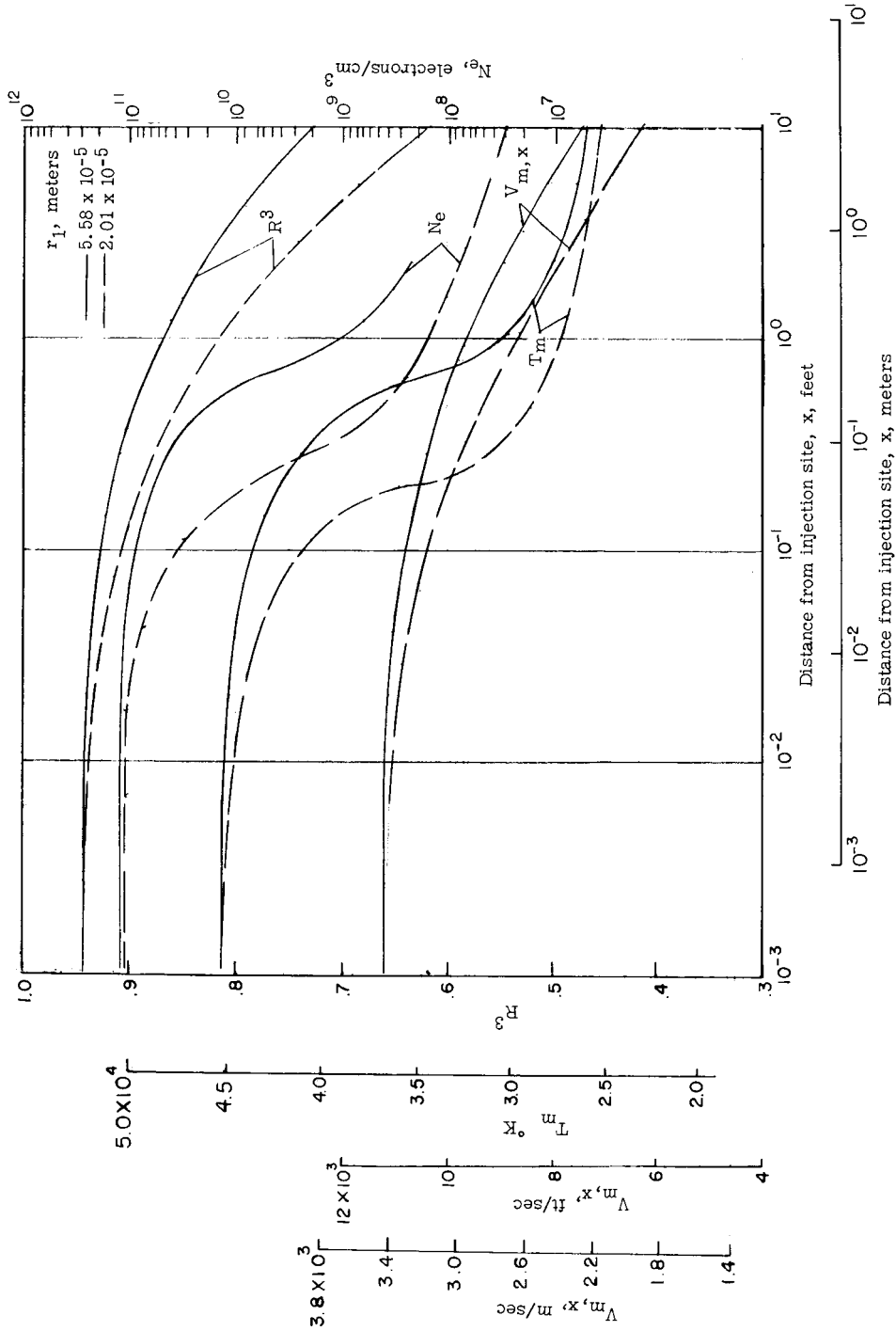
Figure 21.- Schlieren photographs for no injection showing the effect of a change in angle of attack on shock layer thickness.



(a) Altitude 225 000 feet; $p = 5.5$ psf; $\bar{w}_{cr} = 3.0$; $T_{m,1} = 8900^\circ R$; $V_{m,x,1} = 12\ 610$ ft/sec.

Figure 22.- Computed variation of mixture temperature T_m weight fraction of water in liquid phase R_2 , and equilibrium electron concentration N_e by method of reference 7.

UNCLASSIFIED

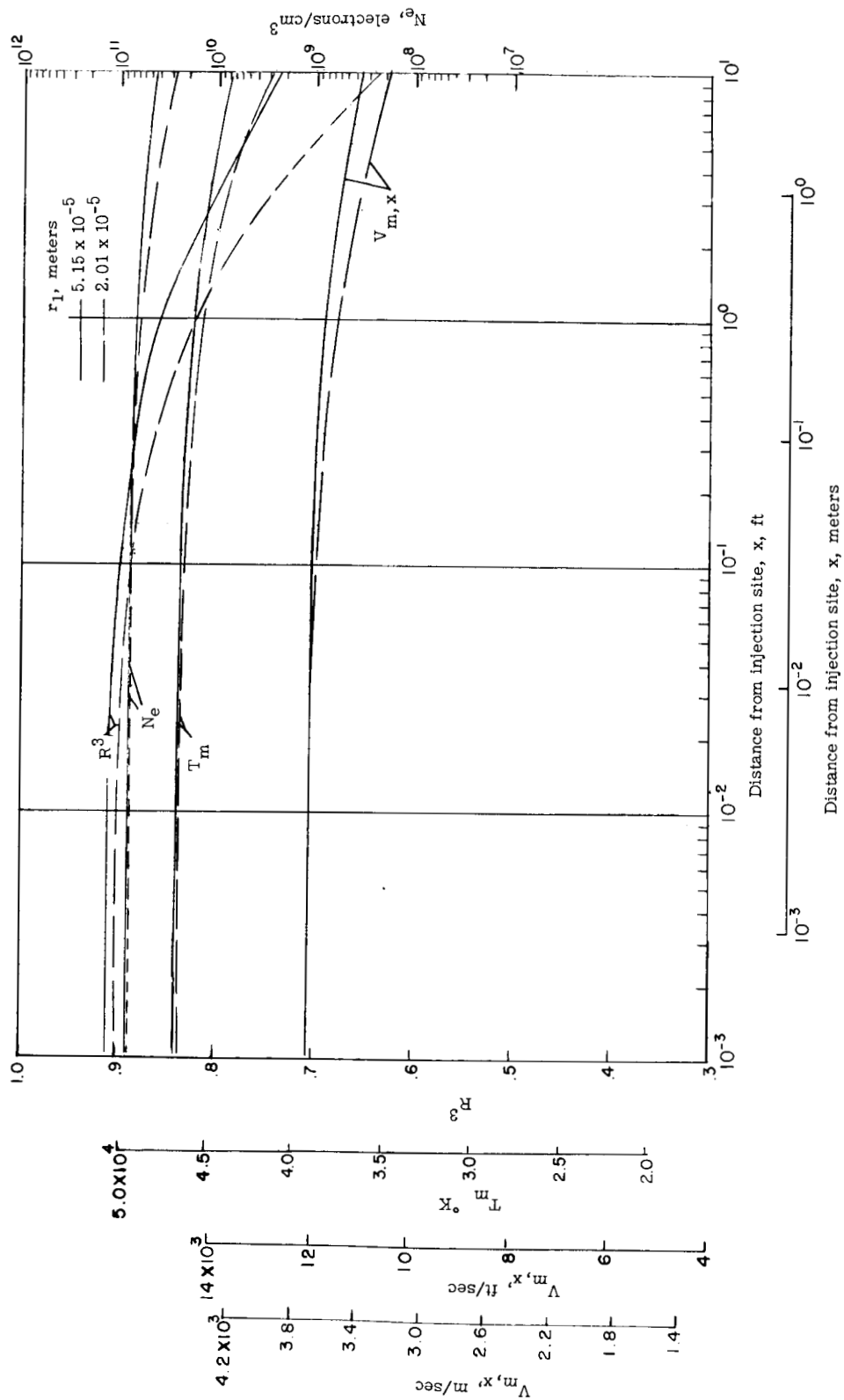


(b) Altitude 246 000 feet; $p = 2.4$ psf; $\bar{w}_{cr} = 2.0$; $T_{m1} = 8640^\circ R$; $V_{m,x,1} = 12\ 730$ ft/sec.

Figure 22.- Continued.

UNCLASSIFIED

UNCLASSIFIED



(c) Altitude 262 000 feet; $p = 1.0$ psf; $\bar{W}_{cr} = 0.5$; $T_{m1} = 8632^\circ R$; $V_{mx,1} = 12\ 790$ ft/sec.

Figure 22.- Concluded.

UNCLASSIFIED

UNCLASSIFIED

~~CONFIDENTIAL~~

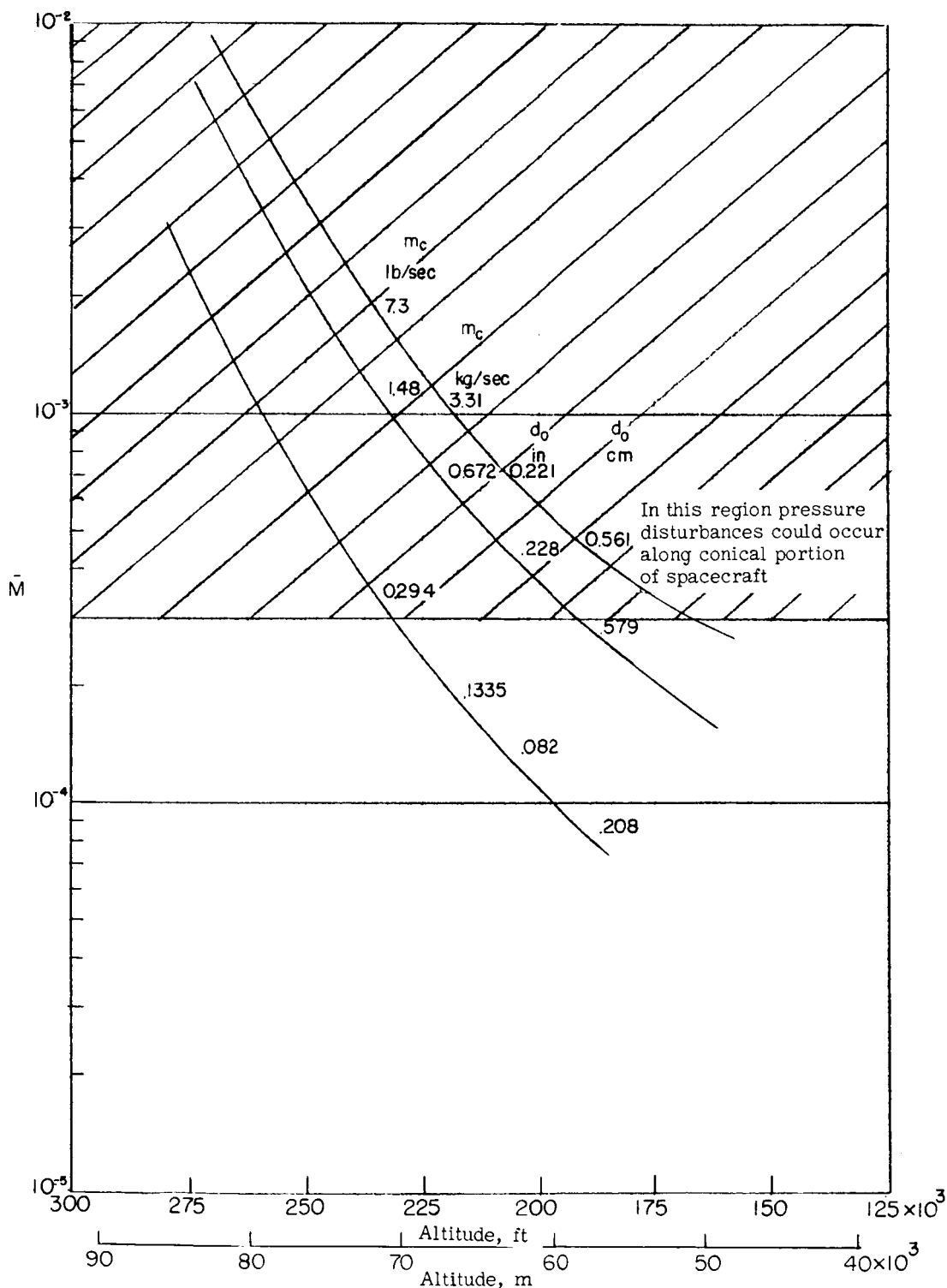


Figure 23.- \bar{M} variation with altitude for GT-3 reentry for three design nozzles.

UNCLASSIFIED

UNCLASSIFIED

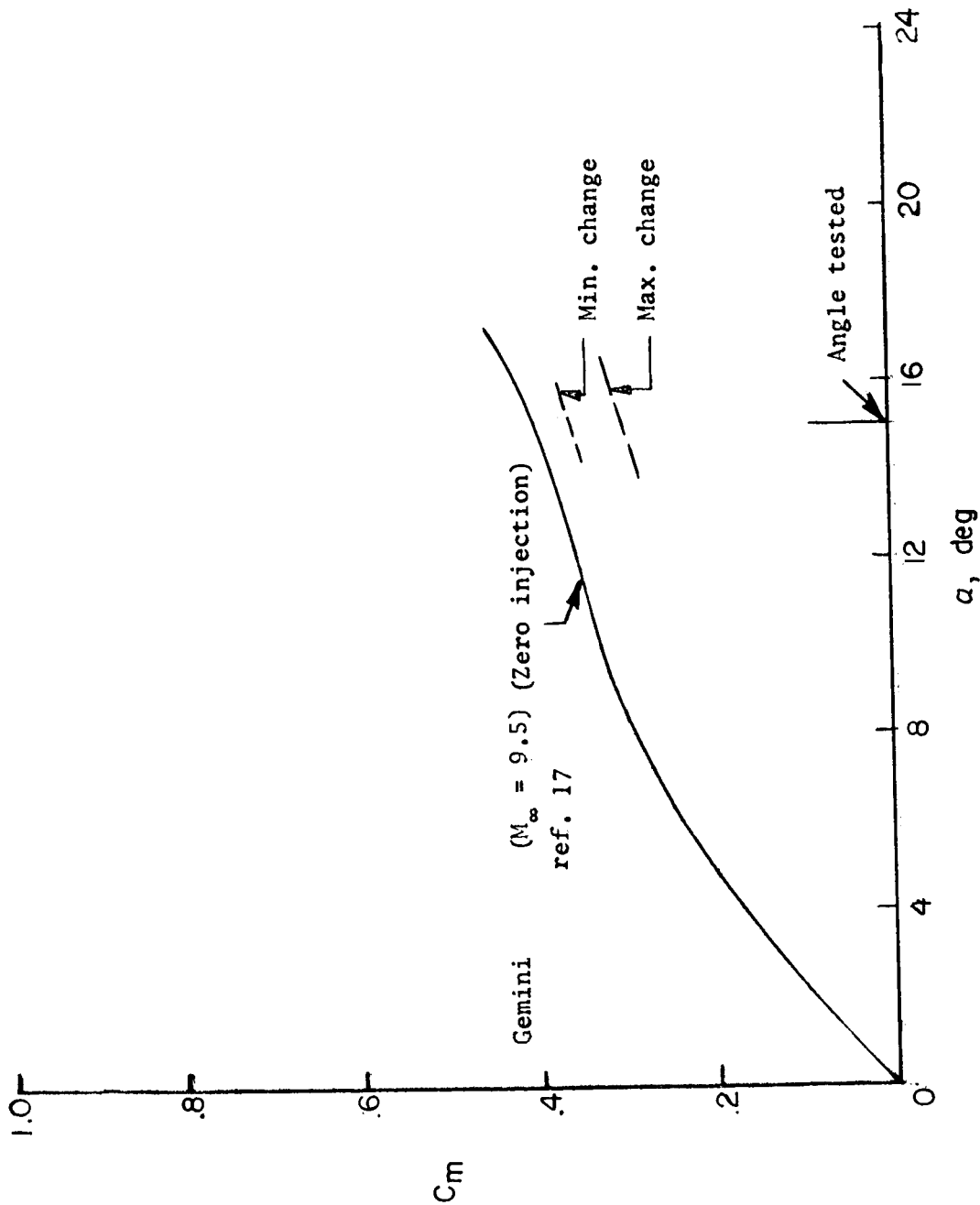


Figure 24.- Effect of injection on pitching-moment coefficient of Gemini reentry configuration. Axial location of center of gravity from heat-shield shoulder was 0.42D.

UNCLASSIFIED

~~CONFIDENTIAL~~

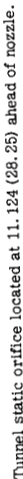


Figure 25.- Sketch of tunnel-wall water injection system showing nozzle details and installation. Dimensions are given in inches and parenthetically in centimeters.

UNCLASSIFIED

UNCLASSIFIED

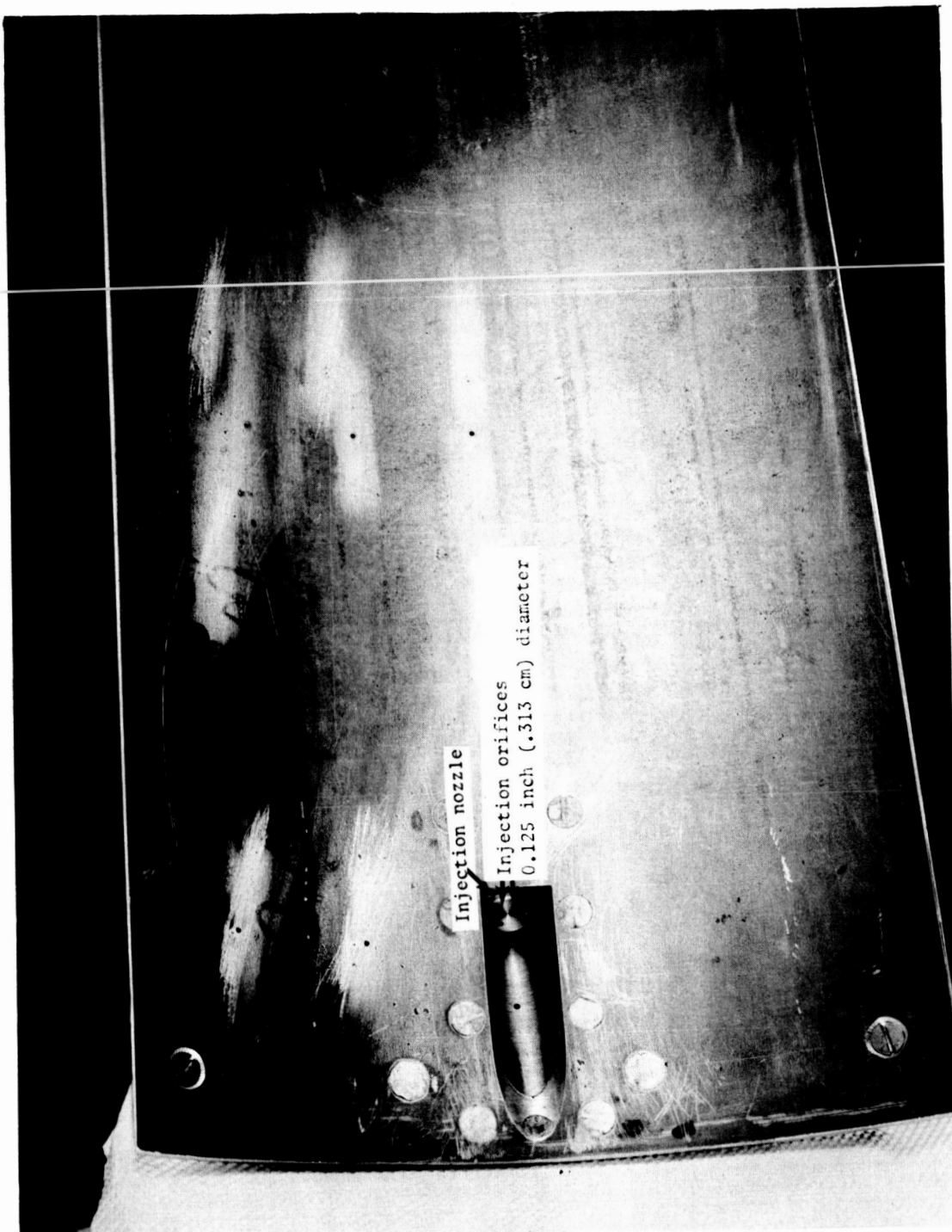


Figure 26.- Photograph of injection plate showing recessed nozzle installation. The nozzle L-64-3230.1 shown has two 0.125-inch-diameter (0.313 cm) orifices. The three holes near the periphery of the nozzle face are for a spanner wrench.

UNCLASSIFIED

UNCLASSIFIED

~~CONFIDENTIAL~~

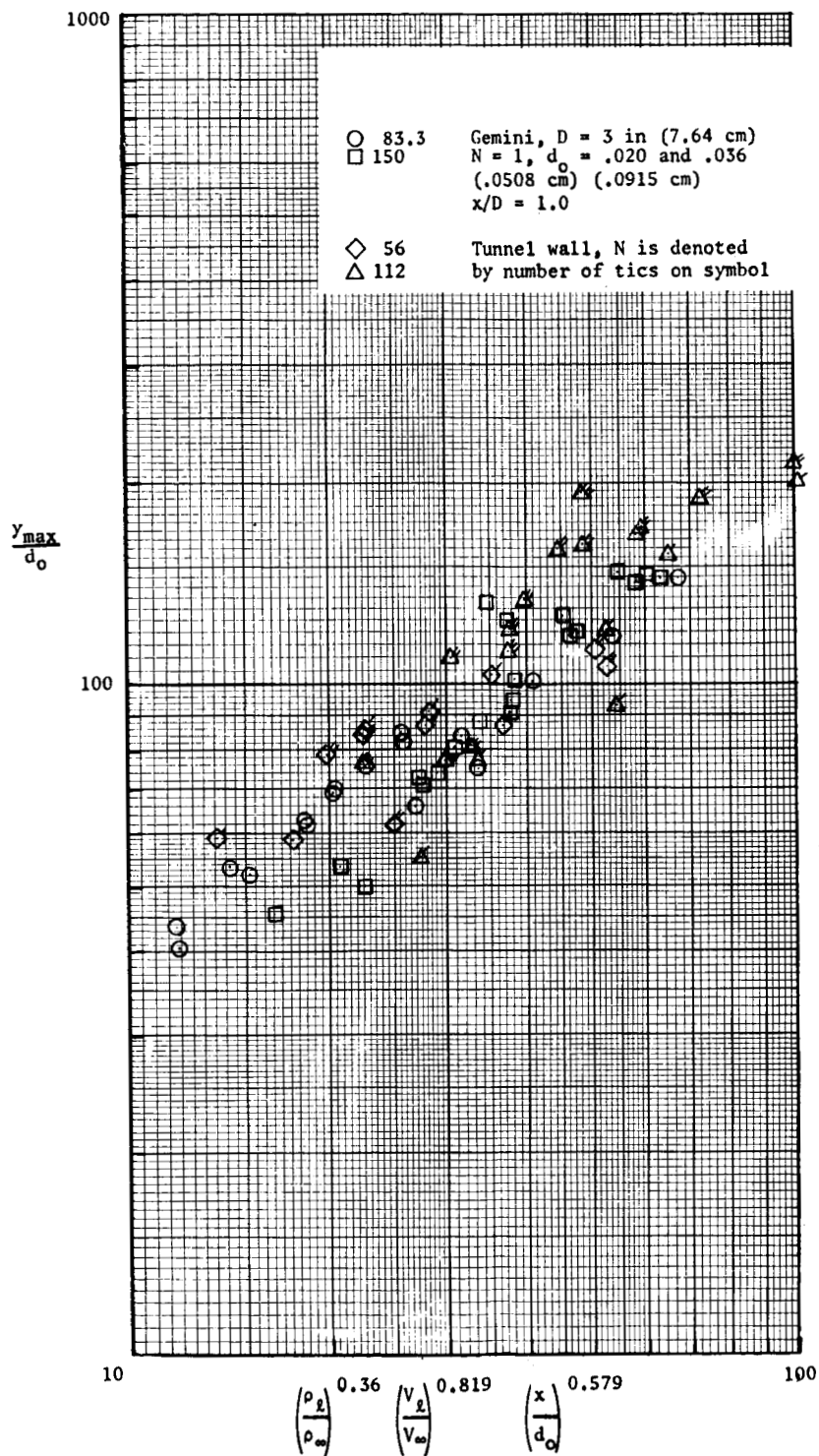


Figure 27.- Correlation of maximum crosscurrent spray penetration from the Gemini model injection ($N = 1$) and the tunnel wall injection ($N = 1, 2$, or 3).

UNCLASSIFIED

~~SECRET~~
UNCLASSIFIED

"The aeronautical and space activities of the United States shall be conducted so as to contribute . . . to the expansion of human knowledge of phenomena in the atmosphere and space. The Administration shall provide for the widest practicable and appropriate dissemination of information concerning its activities and the results thereof."

— NATIONAL AERONAUTICS AND SPACE ACT OF 1958

NASA SCIENTIFIC AND TECHNICAL PUBLICATIONS

TECHNICAL REPORTS: Scientific and technical information considered important, complete, and a lasting contribution to existing knowledge.

TECHNICAL NOTES: Information broad in scope but nevertheless of importance as a contribution to existing knowledge.

TECHNICAL MEMORANDUMS: Information received in limited distribution because of preliminary development, classification, or other reasons.

CONTRACTOR REPORTS: Information developed in connection with a NASA contract or grant and released under NASA auspices.

TECHNICAL TRANSLATIONS: Information published in a foreign language considered to merit NASA translation in English.

TECHNICAL REPRINTS: Information derived from NASA activities and initially published in the form of journal articles.

SPECIAL PUBLICATIONS: Information derived from or of value to NASA activities but not necessarily showing the results of individual NASA-programmed scientific efforts. Publications include conference proceedings, monographs, data compilations, handbooks, sourcebooks, and special bibliographies.

Details on the availability of these publications may be obtained from:

SCIENTIFIC AND TECHNICAL INFORMATION DIVISION
NATIONAL AERONAUTICS AND SPACE ADMINISTRATION

Washington, D.C. 20546

UNCLASSIFIED
~~SECRET~~